The intrinsically disordered N-terminus of the voltage-dependent anion channel

Jordane Preto[a]*, and Isabelle Krimm[a,b]

[a]Université Claude Bernard Lyon 1, Centre de Recherche en Cancérologie de Lyon, INSERM 1052, CNRS 5286, Lyon, France

[b]CRMN, Université de Lyon, CNRS 5280, ENS de Lyon, 5 Rue de La Doua, F-69100, Villeurbanne, France.

* Corresponding author. E-mail: jordane.preto@univ-lyon1.fr

Abstract. The voltage-dependent anion channel (VDAC) is a critical β-barrel membrane protein of the mitochondrial outer membrane, which regulates the transport of ions and ATP between mitochondria and the cytoplasm. In addition, VDAC plays a central role in the control of apoptosis and is therefore of great interest in both cancer and neurodegenerative diseases. Although not fully understood, it is presumed that the gating mechanism of VDAC is governed by its N-terminal region which, in the open state of the channel, exhibits an α-helical structure positioned midway inside the pore and strongly interacting with the β-barrel wall.

In the present work, we performed molecular simulations with a recently developed force field for disordered systems to shed new light on known experimental results, showing that the N-terminus of VDAC is an intrinsically disordered region (IDR). First, simulation of the N-terminal segment as a free peptide highlighted its disordered nature and the importance of using an IDR-specific force field to properly sample its conformational landscape. Secondly, accelerated dynamics simulation of a double cysteine VDAC mutant under applied voltage revealed

metastable low conducting states of the channel representative of closed states observed experimentally. Related structures were characterized by partial unfolding and rearrangement of the N-terminal tail, that led to steric hindrance of the pore. Our results indicate that the disordered properties of the N-terminus are crucial to properly account for the gating mechanism of VDAC.

Author summary. The voltage-dependent anion channel (VDAC) is a membrane protein playing a pivotal role in the transport of ions or ATP across the mitochondrial outer membrane as well as in the induction of apoptosis. At high enough membrane potential, VDAC is known to transition from an open state to multiple closed states, reducing the flow of ions through the channel and blocking the passage of large metabolites. While the structure of the open state was resolved more than a decade ago, a molecular description of the gating mechanism of the channel is still missing. Here we show that the N-terminus of VDAC is an intrinsically disordered region and that such a property has a profound impact on its dynamics either as a free peptide or as part of the channel. By taking disordered properties of the N-terminus into account, we managed to generate long-lived closed conformations of the channel at experimental values of the membrane potential. Our results provide new insights into the molecular mechanism driving the gating of VDAC.

1. Introduction

The voltage-dependent anion channel (VDAC) is a major porin located in the mitochondrial outer membrane (MOM). One of VDAC's main function is to mediate the transport of ions or small metabolites such as ATP, ADP or NADH between the mitochondrial intermembrane space (IMS) and the cytoplasm thus contributing to cell homeostasis (1). In addition, the channel is responsible for alteration of the permeability of the MOM which may result, under

48 specific stimuli, to the release of apoptogenic factors like cytochrome C from the IMS, even-
49 tually leading to apoptosis (2). Through its ability to interact with a dozen different proteins –
50 including itself – VDAC was shown to either induce or inhibit apoptosis depending on its in-
51 teraction partner (2). For this reason, VDAC is usually considered a promising target not only
52 for cancer treatment but also in neurodegenerative diseases where the main goal is to prevent
53 early stages of neuron's death (3).

54 Single-channel conductance experiments have revealed that VDAC can either be found
55 in an open, high conducting, state prevailing at low membrane potential (between -30 mV
56 and 30 mV) or in multiple closed, low conducting, states occurring at more extreme voltage
57 (above or below ± 30 mV) (4, 5). Importantly, anion selectivity can be fairly high in the open
58 state with an anion/cation ratio of 5-6 at 150 mM KCl concentration while closed states were
59 reported to be cation selective (5, 6). Although the structure of the open state of VDAC was
60 resolved more than a decade ago, little is known regarding the structure of the closed states due
61 to their transient properties in normal conditions (4).

62 Experimental structures of the open state of VDAC were first released in 2008 by three
63 separate groups using X-ray crystallography and/or NMR (7-9). VDAC is composed of 19 β-
64 strands forming the barrel as well as an α-helical N-terminus (residues M1 to G25) located
65 midway inside the pore and interacting with the barrel mostly via hydrophobic contacts (Fig
66 1). While the structure of the β-barrel was similar in all cases, slight differences in the position
67 and in the α-helical content of the N-terminus, i.e., long helix vs. small helix vs. helix-break-
68 helix, were observed between published structures (10). Although the N-terminus was reported
69 to be stable in the open state (no large conformational change on the sub-millisecond timescale
70 (11)), these slight variations may be an indicator of local flexibility of that region on longer
71 timescales or different arrangements due to external conditions such as lipid environment (10).
72 The mobility of the N-terminus was confirmed in a wide range of biophysical studies

suggesting that the segment could detach from the pore and even translocate outside the channel during voltage gating (12). Nevertheless, N-terminal translocation does not seem to be required for gating as several experimental studies introducing a disulfide bridge to "lock" the N-terminus against the β-barrel wall showed that closed states may still arise when the segment is located inside the pore (13, 14). Such studies include that of Teijido and al. (14) where the introduction of a S-S bond at L10C-A170C was found to have no effect on the conductance profile of the channel confirming that closure can still be induced without any large conformational change of the N-terminus.

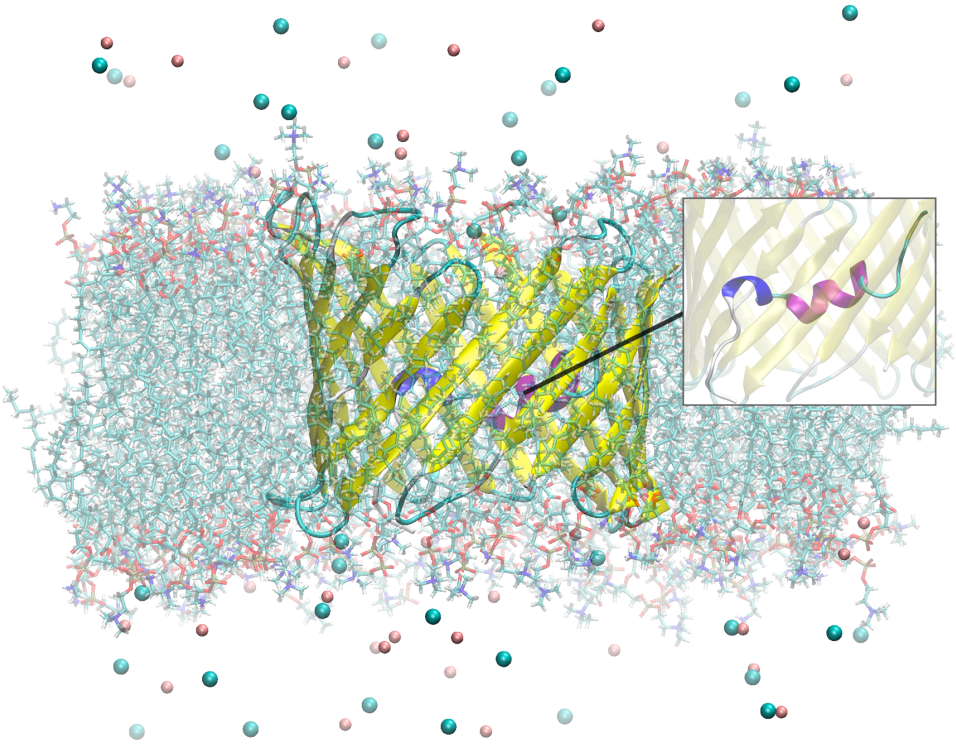

Fig 1. VDAC embedded in a lipid bilayer. The structure of the murine VDAC1 (mVDAC1) solved by X-ray crystallography was used (PDB ID: 3EMN (9)). The inset shows a closer view of the N-terminal region with the 3_{10}-helix involving Y7, A8 and D9, depicted in dark blue, and the standard helix (K12 to T19) in dark pink. Chloride and potassium ions (at a 150-mM KCl concentration) are also shown for illustrative purposes.

Finally, important structural properties of the N-terminus of VDAC were discovered by De Pinto and coworkers (15, 16). Using NMR and circular dichroism (CD) experiments, the

89 authors found that the N-terminal fragment, when produced as a free peptide in solution, was
90 characterized by no apparent structural content. From molecular dynamics (MD) simulations,
91 it was proposed that such a peptide could exist in a dynamic equilibrium alternating between
92 random coil and α-helix content while interaction of the N-terminal region with the inner part
93 of the VDAC barrel would "choose" the α-helix conformation over unstructured ones (16).

94 In the present paper, it is shown that the lack of apparent structure experimentally ob-
95 served by De Pinto and coworkers is a simple illustration of the disordered nature of the N-
96 terminus which, in our opinion, has not properly been investigated until now. By running MD
97 simulations with a force field specifically designed for intrinsically disordered regions (IDR),
98 we showed that the conformational landscape of the N-terminal peptide is mostly unstructured
99 in solution with almost no helical content. Alternatively, simulation with a standard force field
100 similar to what has been used in previous in silico studies, was found to overstabilize its α-
101 helix content leading to erroneous results. Our findings were confirmed by the ability of the
102 IDR force field to reproduce experimental Cα and Cβ chemical shifts both qualitatively and
103 quantitatively, in contrast to the standard force field.

104 In the second part, we explored the importance of the disordered properties of the N-
105 terminus in the gating mechanism of VDAC. Specifically, experiments by Teijido et al. (14)
106 were modeled by introducing a disulfide bond between residues L10C and A170C. Using the
107 IDR-specific force field, accelerated dynamics trajectories at ±40 mV voltage were character-
108 ized by the unfolding of the 3_{10}-helix involving residues Y7, A8 and D9 and subsequent rear-
109 rangements of disordered residues M1 to D9. At +40 mV (*cis* side), the unfolded segment was
110 found to unwind and to move towards the middle of the pore leading to steric hindrance of the
111 channel. Metastable states displaying a low conductance representative of closed states (~50-
112 60% of the conductance in the open state) as well as a reduced anion selectivity, were observed.
113 Specific positioning of the unfolded N-terminal segment in our metastable states as well as the

114 inability for standard force fields to induce stable low-conducting states suggest that the disor-
115 dered properties of the N-terminus are critical to account for the closing mechanism of VDAC.
116 Although our subconducting states were generated at +40mV, the exact role of the membrane
117 potential in channel closure, as compared with random voltage-independent events, is still to
118 be determined.
119

120 ## 2. Results

121 ### 2.1 The N-terminal peptide

122 We first investigated the disordered properties of the N-terminal peptide in solution. Starting
123 from the α-helical N-terminus (M1-G25) directly extracted from the crystal structure of
124 mVDAC1 (9) (PDB ID: 3EMN), we performed μs-long MD simulations using, on one side,
125 the Amber ff14SB force field which is considered one of the standard and latest benchmarks
126 for protein simulations (17) and, on the other side, the ff14IDPSFF force field that was specif-
127 ically designed to sample disordered protein domains (18). Importantly, ff14IDPSFF was re-
128 ported to produce results similar to ff14SB in the case of well-folded systems (18).

129 Representative conformers of the N-terminal peptide obtained after running standard MD
130 with the ff14SB and ff14IDPSFF force fields are shown in Fig 2 (top). Long MD trajectories
131 of 1.6 μs and 2.1 μs were run with ff14SB and ff14IDPSFF, respectively, while convergence
132 was confirmed in both cases as the number of clusters generated from clustering analysis was
133 found to plateau in the last 500 ns (S1 Fig). Notably, important differences in the conforma-
134 tional landscapes of the two force fields were observed. Whereas dynamics performed with
135 ff14SB was mostly characterized by α-helices involving residues Y7 to K20, simulation with
136 the ff14IDPSFF force field led to unstructured conformations including partially as well as
137 fully unfolded structures. To get further insight into the stability of each state, the potential of
138 mean force (PMF) was provided (S2 Fig) as a function of the RMSD with respect to the crystal

structure and the radius of gyration (R_g), two popular collective variables for structural analysis of small peptides (19). As depicted in Fig 2 and S2 Fig, transient secondary structures were also identified using ff14IDPSFF including small antiparallel β-strands made of A2-V3 and Y22-G23 (RMSD~11.5Å, R_g~8.5Å) as well as an α-turn involving D9, L10 and G11 (RMSD~9Å, R_g~9Å). The latter was found to minimally contribute to the overall conformational ensemble (1.24%).

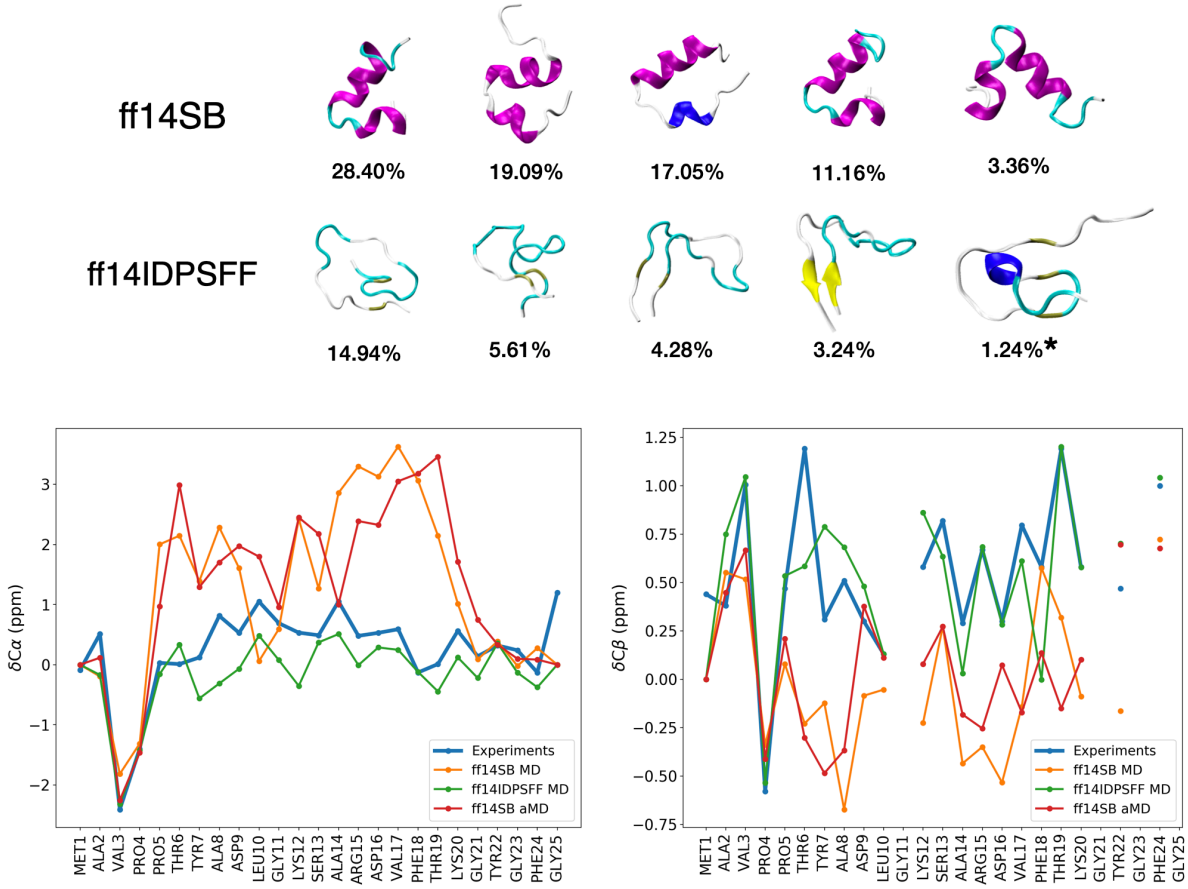

Fig 2. **Representative conformers and chemical shifts of the N-terminal peptide.** Top: representative conformers of the top 5 clusters (and their occupancy) obtained from μs-long simulations with ff14SB and ff14IDPSFF. Note that the last (starred) structure shown for ff14IDPSFF corresponds to the 12th most populated cluster which is the first cluster with α-helical content. Bottom: α- and β-carbons chemical shifts of the N-terminal peptide predicted from molecular simulations and experiments (experimental values were directly extracted from Table S1 in Ref. (16)). Shifts computed from MD simulations were obtained by simple average of the shifts predicted for each generated structure using the SPARTA+ software (20). Shifts

computed from aMD simulations were calculated as weighted averages using Maclaurin series up to rank k=10 in order to approximate the weights (Eq. (4)).

Although our simulations were μs-long and convergence was reached in all cases, we explored the possibility that dynamics carried out with ff14SB could produce other conformations of the peptide (over longer timescales) with no α-helical content. To this purpose, we used accelerated Molecular Dynamics (aMD), a biasing technique originally developed by the McCammon group (21). aMD has been successfully applied to a vast diversity of systems including the 58-residue pancreatic trypsin inhibitor whereby 500ns-long aMD simulation allowed to sample conformations normally reachable on the millisecond timescale (22). Hence, aMD turns out to be a method of choice to investigate the conformational landscape of our 25-residue peptide more thoroughly.

Overall, the conformational landscape generated from a 1μs-long aMD simulation with ff14SB was similar to the α-helix ensemble generated from standard MD using the same force field, with no new basin or new structural content reported (S3 Fig). To eliminate the possibility that our simulations could have been biased by our choice of starting structure, i.e., the α-helical N-terminus extracted from mVDAC1, which may have led to the peptide being "trapped" in an α-helix minimum, we also ran a short aMD simulation (20 ns) starting from a fully unfolded structure ($R_g \sim 20$Å). This time was short enough to observe clear convergence to the main α-helix basin found in our long simulation suggesting that further stable or metastable regions with ff14SB, were unlikely (S3 Fig).

Finally, we investigated the correctness of our results by estimating the NMR chemical shifts of alpha and beta carbons from each simulation and by comparing those values with experimental ones reported elsewhere (16). Results are provided in Fig 2 (bottom) for both ff14SB and ff14IDPSFF force fields where the former is given in cases of standard MD and aMD simulations. Notably, Cα and Cβ chemical shifts predicted using ff14SB were found to

178 be very far from experimental data (chemical shifts obtained from MD and aMD simulations
179 were similar, which is consistent with the similar landscapes observed). Discrepancies were
180 especially visible for α-helix residues confirming the tendency of ff14SB to overexpress sec-
181 ondary structures in disordered systems (23). Conversely, both Cα and Cβ shifts computed
182 from the ff14IDPSFF trajectory showed great agreement with experiments. From S1 Table, we
183 can see that the improvement was both quantitative and qualitative as low RMSE values and
184 high Pearson correlation coefficients (0.870 for Cα and 0.759 for Cβ) were obtained, respec-
185 tively.

186 **2.2 The N-terminus in VDAC**

187 Here we explored the stability of the intrinsically disordered N-terminus as part of the open
188 state of VDAC. MD simulations of mVDAC1 were performed at physiological salt concentra-
189 tion (150 mM KCl) starting from the 3EMN structure (9) embedded in a DOPC/DOPE mem-
190 brane (Fig 1). As with the N-terminal peptide, standard MD was performed with ff14IDPSFF
191 and compared to simulations using the ff14SB force field. Since ff14IDPSFF has not yet been
192 tested on proteins interacting with lipids, the new force field parameters were only applied to
193 the N-terminal region which is located inside the pore, while ff14SB was always used to model
194 the rest of the channel.

195 In Fig 3, we showed the root mean square fluctuations (RMSF) of N-terminal residues
196 over 100 ns while the inset displays the N-terminal RMSD as a function of time. At first glance,
197 we noticed that both force fields resulted in almost equally-rigid N-terminal regions (RMSD <
198 2Å) although many residues including L10 to D16 and Y22 to G25 had a slightly higher RMSF
199 in the case of ff14IDPSFF. Interestingly, this increase in flexibility was not necessarily corre-
200 lated with the ability of secondary structures to unfold. For example, the secondary structure
201 propensity obtained with ff14IDPSFF in the long α-helix (K12 to T19) was equal or even

202 higher than the propensity calculated with ff14SB (S4 Fig). On the opposite, the 3_{10}-helix in-
203 volving Y7, A8 and D9 which is characteristic of the 3EMN structure, was slightly less stable
204 in the case of ff14IDPSFF (0.86 and 0.76 propensity for ff14SB and ff14IDPSFF, respectively).

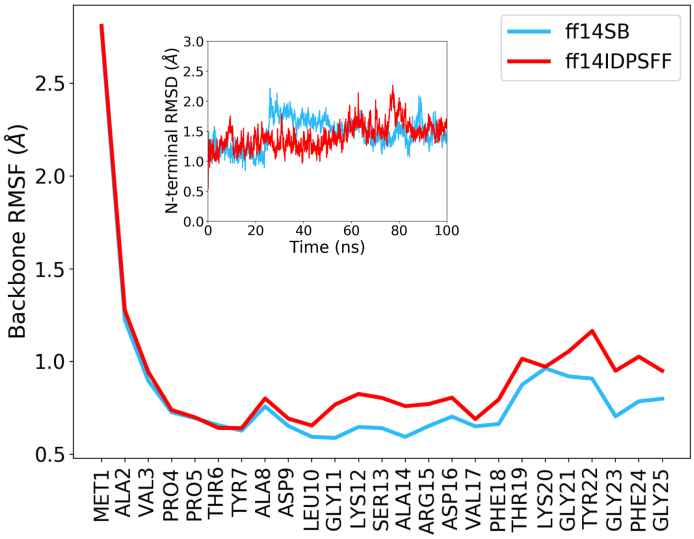

205

206 **Fig 3. RMSF and RMSD of the N-terminus of wild-type mVDAC1**. RMSF and RMSD were computed
207 from 100ns-long runs using ff14SB or ff14IDPSFF. Only the backbone atoms of the N-terminus were con-
208 sidered for the calculation of RMSF. Inset: N-terminal RMSD with respect to the 3EMN structure as a func-
209 tion of time. RMSD values were calculated by first aligning the structures over all the heavy atoms including
210 atoms of the pore and of the N-terminus.

211 Overall, we found that the ff14IDPSFF force field predicted a stable and well-folded N-
212 terminal region within the time frame of our standard MD run (650 ns, see S2 Table) with no
213 apparent transition or change in structural content compared to the 3EMN structure (S1 Video).
214 Not only is this result consistent with experiments showing the stability of the N-terminus in
215 the open state of VDAC (24) but it also confirms the ability of ff14IDPSFF to model stable
216 IDRs as they fold upon interaction with other protein domains.

217 **2.3 Double cysteine mutant**

218 To investigate the closing mechanism of VDAC, simulations of a double cysteine mutant
219 (mVDAC1-Cys) characterized by a disulfide bond connecting residues L10C and A170C, were

220 performed. Electrophysiological measurements by Teijido et al. (14) have revealed that this
221 modification was not altering the gating properties of the channel even though the N-terminus
222 was affixed against the barrel. Therefore, such a setup provides a good way to investigate clo-
223 sure of VDAC from molecular simulations as the presence of the S-S bond should dramatically
224 restrict the exploration of the conformational space of the N-terminus, thereby saving a lot of
225 computational time. In addition, our results should confirm that closure of the channel is not
226 necessarily induced by large conformational changes of that region.

227 All our simulations were initiated from the 3EMN structure where we mutated residues
228 L10 and A170 to create the disulfide bond. Since L10 and A170 were already spatially close
229 to each other in 3EMN (min. interatomic distance ~ 3.9Å), the mutated channel was found to
230 relax to a state similar to the crystal structure (Fig 4). As with mVDAC1 WT, standard MD
231 runs – using either ff14SB or ff14IDPSFF – were unsuccessful in simulating conformational
232 transitions of the N-terminus or the barrel. Therefore, aMD simulations were carried out. Three
233 membrane potentials: 0 mV, +40mV and −40 mV, at 150 mM KCl, were considered (one
234 aMD trajectory per potential). Voltage was defined as positive when it was greater at the side
235 opposite to the ends of N- and C-termini in the open state. Importantly, this side was found to
236 correlate with the cytosolic side of the channel that was also shown to correspond to the *cis*
237 side in planar lipid bilayer (PLB) experiments (25, 26). Therefore, the potential values speci-
238 fied in the present work most likely represent potential values set at the *cis* side in PLB exper-
239 iments while setting the *trans* side to 0 mV.

240 aMD simulations were conducted over hundreds of nanoseconds at each voltage (a sum-
241 mary of our simulations including simulation times, is given in S2 Table). While trajectories
242 generated with ff14SB revealed no major displacements or structural changes of the N-termi-
243 nus at 0 mV or at applied potential (S2 Video), simulations with ff14IDPSFF showed more
244 complex dynamics depending on the voltage: aMD trajectories at +40 mV and −40 mV were

both characterized by early unfolding of the 3_{10}-helix involving residues Y7, A8 and D9 (after 20 ns at +40 mV and after 2 ns at -40 mV). At 0 mV, the 3_{10}-helix was more stable although our aMD trajectory also led to unfolding of this region after 160 ns (S3 Video) suggesting that such an event may not be fully induced by the membrane potential. Despite unfolding of the helix, position and orientation of the N-terminus including those of the N-terminal tail (M1 to T6) remained globally unchanged at 0 mV (S5 Fig) as evidenced by hydrogen bonds at M1-E121, A2-H122 or P4-N124 prevailing all along our simulation.

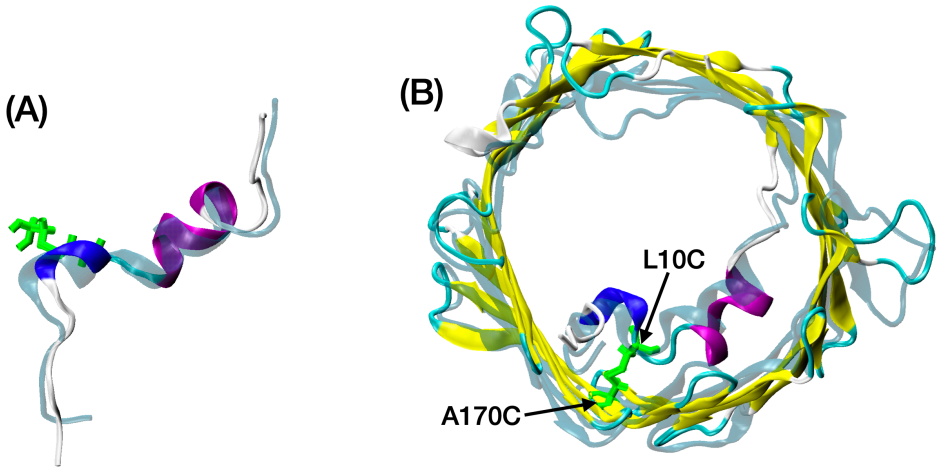

Fig 4. mVDAC1-Cys structure relaxed from 3EMN. mVDAC1-Cys conformation obtained after 10-ns-long equilibration of the (mutated) 3EMN crystal structure using ff14IDPSFF. The crystal structure is depicted in transparent turquoise. Bonded L10C and A170C residues are shown in green. (A) N-terminal region (side view); (B) whole channel (IMS view).

Contrary to the 0 mV case, our +40 mV aMD trajectory showed a detachment of the N-terminal tail from the barrel whereby residues M1 to P5 moved towards the middle of the pore around 140 ns (S4 Video). At this stage, the tail was found to either interact with the β-barrel at strands 4 and 5 (hydrogen bonds at M1-E84, A2-E84), move almost freely or interact with other residues of the N-terminus (hydrogen bonds at M1-D9 and A2-Y7) indicative of a high flexibility of that region (S5 Fig). At −40 mV, we noticed that the N-terminal tail remained in a more "packed-up" conformation (S5 Video, S5 Fig). Although residue M1 was found to

interact electrostatically with E121 just as in the 0 mV case, hydrogen bonds and hydrophobic patch between residues T6, Y7, A8 and strands 7 and 8 were also reported, which led to slight apparent distortion of the barrel in the region of interaction (Cluster #1 in S5 Fig). Remarkably, while the 3_{10}-helix experienced unfolding and subsequent repositioning at different voltages, the long α-helix made of residues K12 to T19 always remained stable and well-folded with a position similar to that of the crystal structure (S5 Fig).

To investigate whether any of the conformations generated from aMD could correspond to closed states of VDAC, we performed grand canonical Monte Carlo/Brownian dynamics (GCMC/BD) which enable to rapidly simulate the flow of ions across membrane channels (27) GCMC/BD has been successfully applied to porin systems (28) including the open state of VDAC (29). In GCMC/BD, only ions are explicitly simulated while the rest of the system including the protein and the membrane, is modeled as a fixed continuous dielectric. In the present study, clustering analysis was carried out on each aMD trajectory (0 mV, +40 mV and −40 mV) by generating 500 clusters in each case. Next, independent GCMC/BD trajectories were run at 150 mM KCl from the representative structure of each cluster to approximate the conductance and anion/cation ratio of each state. Estimates were obtained by running GCMC/BD at a single voltage value for each frame (at +40 mV for frames generated at +40 mV and 0 mV, and at −40 mV for frames extracted from the −40 mV trajectory).

From this approach, we observed that the conductance of the channel remained globally stable at 0 mV with an average value of 0.918 nS and few conformations below 0.6 nS (S6 Fig). Importantly, this mean value was relatively close to the experimental conductance value of the open state of 0.81 nS at 150 mM KCl concentration (6). As another remark, no visible change in the conductance was reported after unfolding of the 3_{10}-helix (160 ns) confirming that the channel was still in its open state after such an event. Regarding the anion/cation ratio, experiments have estimated it to be around 5-6 in the open state of the wild-type VDAC1 at

150 mM KCl (6). In our simulation, large fluctuations of this ratio, characterized by high values (> 40) and an average value of 14, were reported. We speculate that such high ratios are due to the small number of cations crossing the pore during our GCMC/BD runs (often less than 5), which are expected to lead to an overestimation of the anion selectivity in the open state.

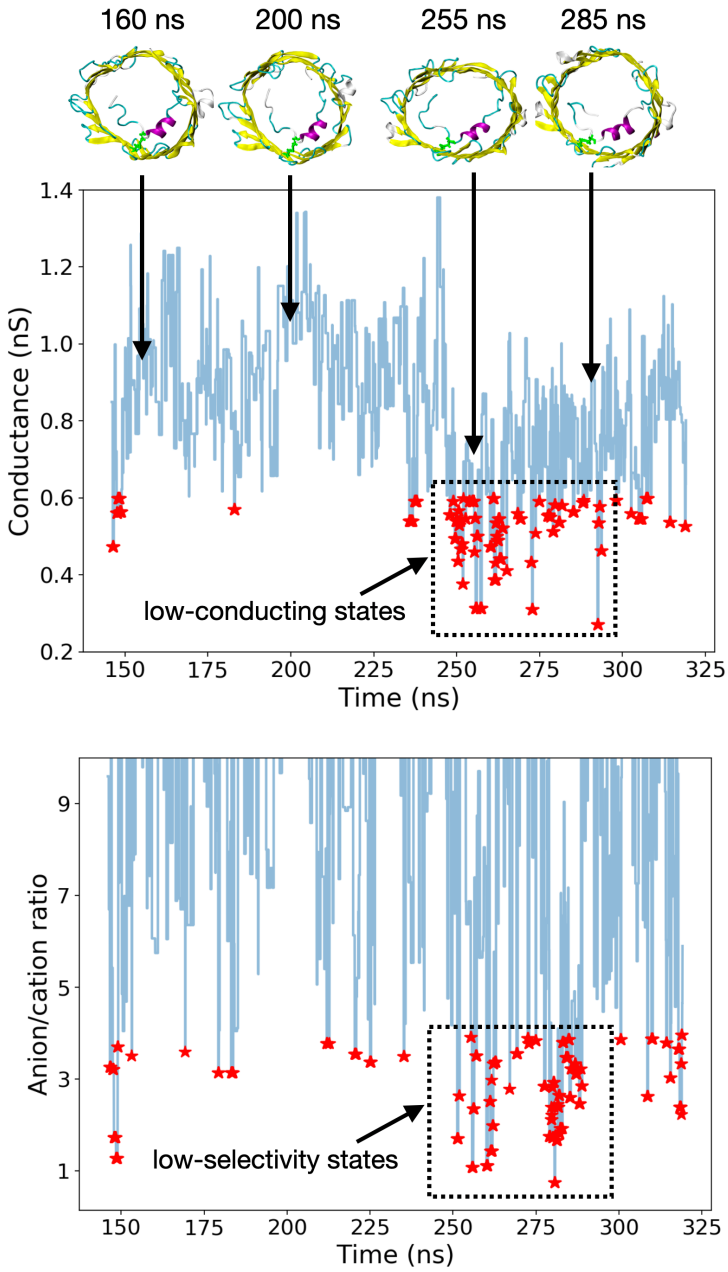

Fig 5. Conductance and anion/cation ratio of mVDAC1-Cys structures generated at +40mV. All values were estimated from GCMC/BD simulations at +40mV (150 mM KCl) performed on 500 representative structures of our +40mV aMD trajectory (once the N-terminal tail has detached and moved inside the barrel

297 (~140 ns)). Time series curves were reconstructed by assigning the same conductance and anion/cation ratio
298 to all the frames of a given cluster. Red stars correspond to all the frames with a conductance less than 0.6
299 nS or an anion/cation ratio less than 4.

300 At +40 mV, our GCBC/BD runs revealed a drop in the conductance at about 250 ns in
301 our aMD simulation with many structures below 0.6 nS (Fig 5), where 0.6 nS corresponds to
302 65.3% of the conductance measured at 0 mV. At this stage, the N-terminus was characterized
303 by a zigzag unfolded segment (from M1 to D9) located midway inside the pore and interacting
304 with the β-barrel mostly via hydrophobic contacts (Fig 5, Cluster #5 in S5 Fig). The drop in
305 the conductance was coupled by a significant decrease in the anion/cation ratio with values less
306 than 3 as well as a few structures exhibiting slight cation selectivity. From 280 ns, conductance
307 slowly increased again which happened when the tail detached again from the barrel. Unlike
308 the +40 mV case, our GCBC/BD simulations performed on our −40 mV aMD trajectory did
309 not show any long-lived subconducting state although a few transient conformations
310 characterized by both a low conductance and reduced anion selectivity or even cation
311 selectivity were observed (S6 Fig).

312 **2.4 Closed state(s)**

313 To investigate the stability of the subconducting conformers generated from aMD at +40mV,
314 standard MD simulations were performed. Out of the 500 representative structures tested using
315 GCMC/BD, 51 frames were predicted to have a conductance less than 0.6 nS between 240 ns
316 and 290 ns (red stars in the dashed rectangle in Fig 5 (top)) and were therefore used as starting
317 point for 200ns-long MD runs at +40mV (one trajectory per conformer). For each trajectory,
318 the electric current was estimated by monitoring the total number of ions crossing the channel
319 and by estimating the slope of the *crossing-events-vs-time* curve from linear regression. As is
320 well known, standard MD tends to overestimate the diffusion coefficient of ions in explicit
321 solvent (29). Hence, a multiplicative factor based on both experimental and simulated bulk

322 diffusion coefficients of potassium chloride was used to compute the current (see section 4.8).
323 As a control, our approach was applied to a 450ns-long MD trajectory of our initial mVDAC1-
324 Cys structure equilibrated from 3EMN (Fig 4). The predicted current was 34.98 pA at +40mV
325 resulting in an (approximated) conductance of 0.87 nS which is well in line with the experi-
326 mental value of 0.81 nS reported in the open state. At the same time, the anion/cation ratio was
327 found to be 5.96 at the end of the simulation which is also quite consistent with the 5-6 ratio
328 observed in experiments.

329 Regarding our subconducting conformers, a summary of the results is provided in S3
330 Table. Among the 51 structures, five were shown to exhibit both a low conductance (around
331 0.6 nS or less) and a reduced anion/cation ratio (around 4 or less). With a pairwise RMSD of
332 1.76 Å, two of the five conformers were found to correspond to the same structural state now
333 referred to as S1 state, while the remaining three also belonged to the same S2 state (see S7
334 Fig). Since the S1 state displayed a lower apparent conductance (~ 0.5 nS) and anion/cation
335 ratio (< 3) than S2, we chose to investigate the former more thoroughly by extending the tra-
336 jectory of one such conformer up to 450 ns at +40mV and by comparing the results with those
337 of the open state. The number of crossing events as well as the anion/cation ratio are shown in
338 Fig 6 for the open state and S1. In both cases, we noticed that the number of crossing events
339 described an almost straight line as a function of time confirming the stability of each state in
340 terms of conductivity. The ratio of crossing events between S1 and the open state was 96/167
341 ~57.5%, at the end of the simulation which falls within the range of conductance ratios reported
342 experimentally and is consistent with our previous GCMC/BD runs. The anion/cation ratio in
343 S1 was also in line with our GCMC/BD simulations (2.7 at 450 ns) indicating a higher prefer-
344 ence for cations although no full cation selectivity was observed (the ratio was always greater
345 than 1).

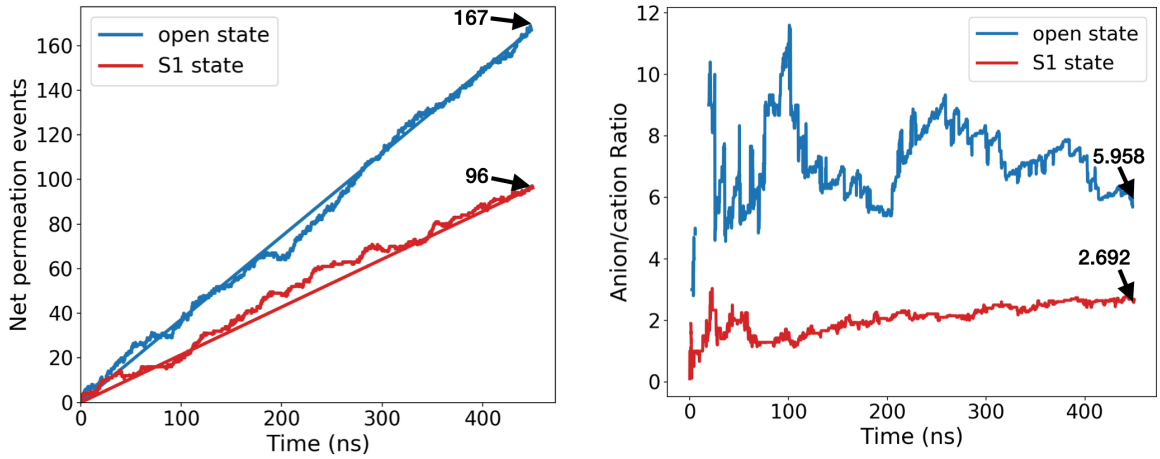

Fig 6. Net permeation events and anion/cation ratio in mVDCA1-Cys open state and subconducting S1 state. Values were obtained from 450ns-long standard MD trajectories at +40mV. In the figure showing net permeation events, the line connecting the first and last points was plotted, the slope of which can be used to estimate the electric current (section 4.8).

Finally, we explored the structural origin of the low conductance and anion/cation ratio in the S1 state. Note that our 450 ns-long MD trajectories of the open and S1 states can be seen from S6 and S7 Videos, respectively. Interestingly, trajectory of the S1 state revealed a flexible N-terminal tail (M1 to P5) with different positions and orientations: e.g., the segment was initially pointing toward the cytosolic side while it was more oriented toward the IMS at the end of the trajectory. As the electric current was found to be stable until the end of the simulation (Fig 6), this suggests that residues M1 to P5 are unlikely to fully account for the low conductance. Alternatively, subsequent residues (T6 to D9) always displayed a stable unfolded horizontal position (see also S8 Fig) interacting with the β-barrel via hydrophobic contacts whereas the rest of the N-terminus (C10 to G25) was structurally similar to that of the open state (Fig 7 (A)). Involvement of residues T6 to D9 in the electric current flow was also visible from the density profile of chloride permeation events. This density profile is shown in Fig 7 (B) and Fig 7 (C) as a cross section made of all the (x, y) positions of Cl^- ions reaching the middle of the channel. From these figures, we noticed that residues of the unfolded N-terminal segment

obstructed the pore in a steric way in the S1 state as illustrated by the complete disappearance of an anion density peak located close to the 3_{10}-helix in the open state.

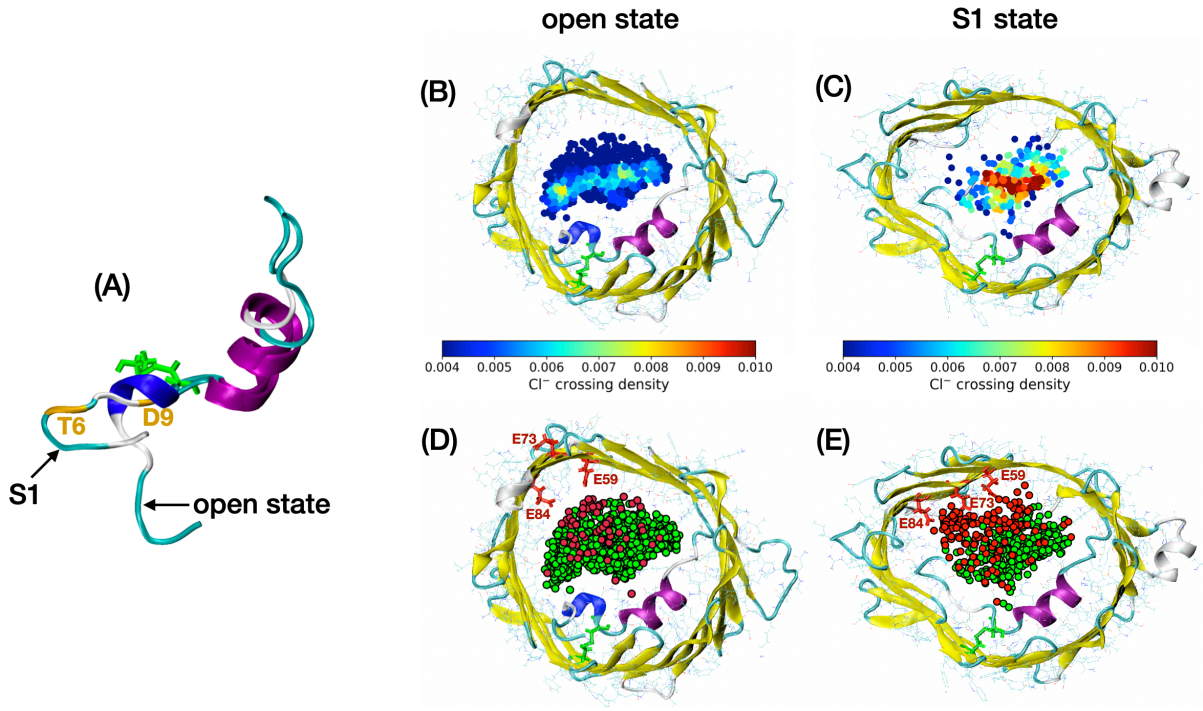

Fig 7. Open state and subconducting S1 state of mVDCA1-Cys. (A) side view of the N-terminal region. (B, C): density profile of chloride ions crossing the middle of the channel in the open state (B) and S1 state (C). Crossing events were collected from our 450ns-long MD trajectories. Note that the density was normalized with respect to the total number of Cl^- crossing events in each case (which is around twice smaller in S1). (D, E): positions of potassium ions (in red) and chloride ions (in green) crossing the middle of the channel in the open state (D) and S1 state (E). The open and S1 conformations correspond to representative structures extracted from each MD trajectory. Bonded L10C and A170C residues are shown in green while E59, E73 and E84 residues are colored in red.

Regarding anion selectivity: since the N-terminus was found to block an anion-enriched region within the pore in S1, it was reasonable to observe a decrease in the anion/cation ratio as well. However, our subconducting trajectory also revealed an increase in cation crossing events with respect to the open state (Fig 7 (D) and Fig 7 (E)). In both states, cations were mostly localized close to the barrel wall opposite to the long helix of the N-terminus as was also reported in previous in silico studies (30). Importantly, this region was found to correlate

382 with the positions of three negatively charged residues, namely, E59, E73 and E84, located
383 next to each other on three consecutive strands (β3, β4 and β5). In S1, the K^+ density became
384 higher in this area where we noticed that the side chain of E73 had shifted into the pore while
385 originally pointing toward the membrane (Fig 7 (E)). Notably, E73's reorientation initially oc-
386 curred in our +40mV aMD trajectory at 70 ns (i.e., before detachment of the N-terminal tail)
387 but was not observed in our aMD runs at 0 mV or -40mV. In this configuration, the side chains
388 of three consecutive residues T72, E73, K74 are facing the pore region which may seem unex-
389 pected as consecutive residues in β-sheets usually alternate between each side of the protein
390 backbone. However, E73's new orientation remained unchanged until the end of our aMD tra-
391 jectory as well as in subsequent hundreds-ns-long MD simulations at +40mV confirming its
392 stability at this voltage. Although E73 reoriented early on in our aMD trajectory, decrease in
393 anion selectivity was only observed for a few specific conformers (Fig 4 bottom) suggesting
394 that reorientation of E73 was not sufficient to guarantee cation preference.

395 **3. Discussion**

396 In the present study, the intrinsically disordered nature of the N-terminus of VDAC as well as
397 its importance in the gating mechanism of the channel were explored. Although not fully
398 acknowledged until now, several arguments in favor of an intrinsically disordered N-terminal
399 segment in VDAC can be put forward: (i) using NMR and CD techniques, De Pinto and
400 coworkers have shown that a free peptide corresponding to such a domain mostly exists as a
401 random coil in solution (15, 16). As the N-terminus of VDAC is known to translocate out of
402 the pore of the channel in specific environmental conditions (12), it was suggested that N-
403 terminal unstructured properties were essential in the interaction of VDAC with other proteins
404 (16); (ii) closer look at the sequence of the N-terminal domain reveals that 13 (out of 25) resi-
405 dues belong to the well-known eight disordered-promoting residues, namely, G, A, S, P, R, Q,
406 E and K. Such residues were originally identified from analysis of various X-ray, NMR and

407 CD data, as being more prevalent in disordered segments (31). In VDAC, disordered-promot-
408 ing residues specifically include A8, G11, K12, S13, A14 and R15, six amino acids involved
409 in the α-helix domain of the N-terminus in the open state; (iii) application of disorder-predic-
410 tion software like s2D (32) or ESpritz (33) predicted that the N-terminus of VDAC1 was es-
411 sentially disordered although the s2D method also revealed a propensity of residues K12 to
412 T19 to form helices (S9 Fig). In the case of ESpritz, all the N-terminal residues were predicted
413 to be disordered (i.e., they were all classified as "D") irrespective of the choice of the training
414 set (X-ray or DisProt); (iv) a feature of many disordered systems is that they can fold into
415 different structures when binding to other proteins or protein domains (34). Interfaces which
416 are crucial to stabilize secondary structures were reported to be significantly more hydrophobic
417 than those of globular protein complexes (35). In the open state of VDAC, the vast majority of
418 interactions between the helical N-terminus and the β-barrel are non-polar (9). These include
419 the well-known hydrophobic patch between L10 and V143-L150 that was shown to be highly
420 conserved across species (8, 9).

421 Along with the above arguments, further evidence of the disordered properties of the N-
422 terminus of VDAC was provided in the present work where MD performed with the IDR-
423 specific ff14IDPSFF force field enabled to reproduce experimental chemical shifts of the free
424 N-terminal peptide while the standard ff14SB force field was unsuccessful in doing so. From
425 a structural point of view, simulations with ff14SB were characterized by a significant amount
426 of helical content that was most likely responsible for the large deviation from experimental
427 values. Importantly, the tendency of popular force fields to overstabilize secondary structures
428 in disordered systems is not new and is due to force field parameters, especially dihedral cor-
429 rection terms, which are normally calibrated from databases of well-folded proteins (36-38).
430 Such force fields include ff14SB, CHARMM27 and ff99SB which have been extensively used
431 in previous in silico studies on VDAC (16, 39-41). Conversely, our simulation with the IDR-

432 specific force field showed almost no α-helical content in the free peptide aside from a small
433 α-turn made of D9, L10 and G11. The complete absence of an α-helical segment similar to the
434 one observed in the crystal structures of VDAC indicates that the α-helix pattern specific of
435 the open state is formed via induced folding through interaction with the β-barrel and not via
436 conformational selection as previously presumed (16). Moreover, the ability of ff14IDPSFF to
437 properly simulate well-folded systems was confirmed by our MD simulations of mVDAC1 in
438 its open state whereby the N-terminus remained stable all along a 650ns-long trajectory. Aside
439 from ff14IDPSFF, other force fields have been recently developed to account for intrinsic dis-
440 ordered segments in proteins such as the CHARMM36m force field (42) although their level
441 of accuracy may vary depending on the system being studied (43). Therefore, application of
442 other force fields to VDAC N-terminus should require preliminary validation, e.g., from a com-
443 parison with experimental shifts as we have done in the present work.

444 In the second part, we investigated whether the disordered properties of the N-terminus
445 were of importance for the gating mechanism of VDAC. This was done by running aMD sim-
446 ulations on a double cysteine mutant (mVDAC1-Cys) characterized by a disulfide bridge con-
447 necting residues L10C and A170C. As shown by Teijido et al. (14), such a setup enabled to
448 induce closed states of the channel while affixing part of the N-terminus against the barrel, thus
449 restricting the exploration of the conformational landscape. Just like the free peptide, striking
450 differences between the ff14SB and ff14IDPSFF force fields were noticed. Whereas the N-
451 terminus of VDAC with ff14SB was insensitive to a +40 mV voltage (no conformational or
452 structural change observed), aMD simulation with ff14IDPSFF showed that the N-terminal tail
453 (M1 to T6) could detach from the β-barrel subsequent to unfolding of the 3_{10}-helix (Y7, A8
454 and D9). The tail was found to move further inside the pore while the long α-helix (K12 to
455 T19) remained folded and stably interacting with the barrel all along our simulation. As the N-
456 terminal peptide was shown to lose its secondary structure in solution, the stability of the long

457 helix in mVDAC1-Cys may be explained by the presence of the C10-C170 disulfide bond
458 whereby residues K12 to T19 are constrained to interact with the barrel thus preserving helical
459 content in this region. Next, using GCMC/BD simulations performed on representative struc-
460 tures generated using ff14IDPSFF, we managed to identify a large number of conformers char-
461 acterized by a low conductance (~50-60% or below of the conductance in the open state).

462 Stability of our subconducting conformers was further investigated by running hundred-
463 ns-long standard MD trajectories using each structure as a starting point. From our analysis,
464 we identified five frames showing long-lived subconducting behavior together with a reduced
465 anion/cation ratio. The five frames were found to be divided into two different structural states,
466 namely, S1 and S2, characterized by different arrangements of the unfolded M1-C10 segment
467 although, in both cases, the segment was interacting with the barrel midway inside the pore.
468 Remarkably, our stable subconducting structures were all reported to match either the S1 or S2
469 states suggesting that the low conductance was mainly due to the specific positioning of the N-
470 terminus even though such arrangements may have a structural impact on the rest of the chan-
471 nel. For example, we observed that the S2 state exhibited slightly higher ellipticity than S1 or
472 the open state (mean ellipticity values were estimated at 0.182, 0.165, 0.143 from S2, S1 and
473 open states trajectories, respectively). While more thorough investigation might be needed to
474 explore whether the ellipticity is partly responsible for the low conductance, the observed in-
475 crease in S2 is still well below that of semicollapsed states reported in (11). Nevertheless, given
476 the multiplicity of VDAC closed states, we leave open the possibility that other stable closed
477 states with higher ellipticity could exist.

478 Aside from ellipticity measurements, we also started to explore the structural origin of
479 the low conductance and the higher cation preference in the S1 state. Closer look at Cl- ions
480 crossing the middle of the pore indicated that the unfolded T6-D9 segment of the N-terminus
481 further reduced the opening of the pore as compared with the open state. The T6-D9 segment

482 remained stable mostly because of hydrophobic contacts with the barrel as shown in S10 Fig.
483 Interestingly, an increase in cation crossing events was also reported in S1 which contributed
484 to lowering the anion/cation ratio. We observed that K+ ions were mostly concentrated close
485 to a negatively charged motif made of residues E59, E73 and E84 where E73's side chain was
486 found to face the pore region. From our analysis, we were, however, unable to determine the
487 exact involvment of E73 in cation permeation or whether E73's reorientation was favored by
488 our membrane potential. Noticeably, a stable salt bridge involving E84 and K115 was also
489 found in the S1 state (S10 Fig) which may also contribute to stabilizing cation-friendly paths.
490 Regarding cation selectivity which seems to be typical of closed states in the wild-type VDAC1
491 (5, 6), none of S1 or S2 were reported to have a anion/cation ratio less than 1. This result may
492 be due to the presence of the disulfide bond which prevents further rearrangement of the N-
493 terminus required for a full cation selectivity (40). For the record, mVDAC1-Cys was found to
494 exhibit typical gating profile in terms of conductance (14), yet no measurement of the an-
495 ion/cation ratio was reported that could confirm cation preference of closed states in that case.
496 Finally, although S1 and S2 were generated from aMD at +40mV, we cannot rule out
497 that such states were generated from random voltage-independent events. To investigate the
498 specificity of S1 at positive voltage, five 200ns-long additional trajectories were run at 0mV,
499 +40mV and -40mV. In each trajectory, the RMSD of the T6-D9 segment with respect to our
500 S1 state was computed since T6-D9 was observed to partially block the chloride flux in S1. At
501 +40 mV, 1 trajectory out of 5 was reported to reach conformers similar to S1 (RMSD < 3.0Å)
502 whereas no such trajectories were found at 0 mV or -40 mV (RMSD > 4.0Å). Even though our
503 results might indicate that S1 is typical of a positive voltage, further analysis is required to
504 confirm the real impact of the membrane potential. Another possible scenario being that high
505 enough voltage, either positive or negative, would be especially important to make the N-
506 terminus unfold (even partially) or detach from the barrel, and that transitions to the multiple

closed states would arise in a more random way given the high flexibility of the unfolded N-terminus. In that case, structurally-similar subconducting states may emerge regardless of the positivity of the voltage. Validation of one model over another is beyond the scope of the present paper whose objective was to point out that metastable subconducting states of VDAC can be prevail at realistic voltage values and most likely rely on the disordered properties of its N-terminus.

4. Material and Methods

4.1 MD software and force fields

All our MD simulations, including standard and aMD simulations, were performed using the Amber16 package (45). The ff14SB force field (17). which is known as the latest Amber force field benchmark for proteins simulations is directly available from the Amber package while the ff14IDPSFF force field (18) was obtained from direct request to Prof. Ray Luo's group. ff14IDPSFF can also be downloaded from the Precise Force Field and Bioinformatics Laboratory website: http://cbb.sjtu.edu.cn/~hfchen/index_en.php.

4.2 Structure preparation (peptide)

The N-terminal peptide was obtained by extracting the N-terminal region (M1-G25) from the mVDAC1 structure in the open state (PDB ID: 3EMN (9)). Protonation of the peptide was done using the PropKa algorithm from the MOE 2018 software at a neutral pH (46). Using the Amber's LEaP module, the system was set into an octahedral box filled with TIP3P waters requesting at least a 15Å distance between any atom of the peptide and the box edges. Overall, 8826 water molecules were incorporated into the simulation box. Sodium and chloride ions were added to neutralize the system as well as to approximate a 0.01M concentration consistent with experimental conditions used for NMR chemical shifts measurements (16). Both ff14SB

531 and ff14IDPSFF simulations of the N-terminal peptide were based on the above preparation
532 protocol. However, setting up ff14IDPSFF simulations further required to generate a new to-
533 pology file containing the proper force field parameters (dihedral correction terms). This was
534 done by running the Trans_FF_IDPs.pl script available with the ff14IDPSFF force field using,
535 as an input, the ff14SB topology file generated from the LEaP module (45). For each force
536 field, equilibration of the solvated structure was performed with the Amber's pmemd utility by
537 first minimizing the whole system (peptide and solvent) during 5000 steps using the steepest
538 descent method followed by 5000 steps of conjugate gradient. Next, simulations in the NVT
539 ensemble were carried out for 500 ps by slowly heating the system from 0K to 298K while
540 restraining heavy atoms of the peptide. Lastly, NPT simulations at $P = 1$ bar and $T = 298$K
541 were run without restraints during 500 ps to finalize the equilibration process.

542 **4.3 Production MD (peptide)**

543 Unbiased MD production was conducted during 1.6 μs and 2.1 μs using the ff14SB and
544 ff14IDPSFF force field, respectively. aMD simulations performed with the ff14SB force field
545 were run during 1 μs. Details regarding the aMD method and our protocol are given below.
546 Additional aMD simulations starting from a fully unfolded structure of the peptide were run
547 using the ff14SB force field during 20 ns, which was found to be enough to reach the α-helix
548 basin. In that case, the initial conformation was simply extracted from our ff14IDPSFF simu-
549 lation by selecting the structure with maximum radius of gyration (≥ 20Å).

550 **4.4 Accelerated MD**

551 To efficiently sample the conformational space of the N-terminal peptide and of mVDAC1-
552 Cys, aMD simulations were run. Briefly, aMD is based on adding a non-negative biasing po-
553 tential (boost) to the system whenever the system potential is less than an energy threshold (47)

$$V'(\boldsymbol{x}) = V(\boldsymbol{x}) \quad \text{when } V(\boldsymbol{x}) \geq E$$
$$V'(\boldsymbol{x}) = V(\boldsymbol{x}) + \Delta V(\boldsymbol{x}) \text{ when } V(\boldsymbol{x}) < E, \tag{1}$$

where $V(\boldsymbol{x})$ is the true MD potential, $\Delta V(\boldsymbol{x})$ is the aMD boost and E is the energy threshold. The addition of the $\Delta V(\boldsymbol{x})$ term is done in such a way as to reduce the height of local energy barriers, and is therefore dependent on the energy of the system at $\boldsymbol{x}$. In the present work, aMD was run in its dual boost version, i.e., the aMD boost is the sum of two biasing contributions: one acting on all atoms (including solvent atoms) through the total potential energy $V(\boldsymbol{x})$, and the other one acting only on dihedral angles through the dihedral energy $V_d(\boldsymbol{x})$ such that:

$$\Delta V(\boldsymbol{x}) = \frac{(E_p - V(\boldsymbol{x}))^2}{\alpha_p + E_p - V(\boldsymbol{x})} + \frac{(E_d - V_d(\boldsymbol{x}))^2}{\alpha_d + E_d - V_d(\boldsymbol{x})} \tag{2}$$

Here E_p and E_d correspond to the average (total) potential and dihedral energies of the biased simulations, respectively, whereas α_p and α_d are coefficients accounting for the contribution of each biasing term. Following standard aMD protocols (22,48), the above coefficients were computed from the following formulas:

$$E_p = E_{p,0} + \gamma_p \cdot n_{atoms}, \qquad \alpha_p = \gamma_p \cdot n_{atoms}$$
$$E_d = E_{d,0} + \gamma_d \cdot n_{residues} + \gamma'_d \cdot n_{lipids}, \qquad \alpha_d = 0.2\left(\gamma_d \cdot n_{residues} + \gamma'_d \cdot n_{lipids}\right), \tag{3}$$

where $\gamma_p = 0.16$ kcal/mol/atom, $\gamma_d = 3.5$ kcal/mol/residue and $\gamma'_d = 30.0$ kcal/mol/lipid. n_{atoms}, $n_{residues}$ and n_{lipids} are the number of atoms (including solvent atoms), the number of residues (25 in the case of the peptide) and the number of lipids, respectively. $E_{p,0}$ and $E_{d,0}$ are the average potential and dihedral energies of the unbiased system, respectively, that were estimated from direct analysis of our equilibration simulations in the NPT ensemble.

4.5 aMD reweighting

570 An important feature of aMD is the possibility to recover ensemble averages associated with
571 the true MD profile. As is well known, structures generated from a biased (equilibrated) simu-
572 lation characterized by a biasing potential $\Delta V(\boldsymbol{x})$ can be assigned a weight $\mathrm{w}(\boldsymbol{x})$ accounting
573 for how they really contribute to the unbiased free energy. This weight is given by the Boltz-
574 mann factor: $\mathrm{w}(\boldsymbol{x}) = e^{\Delta V(\boldsymbol{x})/k_b T}$ that enables to compute the average of any collective variable
575 $\xi(\boldsymbol{x})$ as

$$\langle \xi \rangle = \frac{1}{\sum_i \mathrm{w}(\boldsymbol{x}_i)} \sum_i \mathrm{w}(\boldsymbol{x}_i)\xi(\boldsymbol{x}_i) \tag{4}$$

576 where $\boldsymbol{x}_i$ are the coordinates of the structures generated through the biased simulation. Notably,
577 the exponential factors can be expressed as a Maclaurin series (49) such that:

$$\mathrm{w}(\boldsymbol{x}) = \sum_{k=0}^{\infty} \frac{1}{k!} (\Delta V(\boldsymbol{x})/k_b T)^k \tag{5}$$

578 In practice, finite sampling leads to small errors in the distribution of the $\Delta V(\boldsymbol{x_i})$ while
579 high-order terms in the above series contribute to increase that noise. Therefore, it is of com-
580 mon practice to approximate the weights $\mathrm{w}(\boldsymbol{x})$ by keeping only low-order terms. In this work,
581 all averages quantities deduced from our aMD simulations, including chemical shift estima-
582 tions, were computed from Eqs. (4) and (5) by keeping only terms up to $k = 10$. Although
583 widely accepted, we have tested the applicability of the mentioned formulas on a toy model –
584 alanine dipeptide in explicit solvent – by confirming that averages of φ, ψ dihedral angles of
585 the peptide from aMD data could well reproduce averages obtained from standard MD (not
586 shown).

587 **4.6 Chemical shifts**

588 Cα and Cβ chemical shifts were calculated using the SPARTA+ software (20) which relies on
589 a neural network algorithm to predict the shifts from an input protein structure. The high

590 execution speed of the program enabled to compute the chemical shifts for each structure saved
591 throughout our MD or aMD simulations (one structure saved every 2 ns). Standard averages
592 of each chemical shift – or weighted averages in the case of aMD data – were computed from
593 those predictions and directly compared with experimental data (Table S1 in Ref. (16)).

594 **4.7 Structure preparation (channel)**

595 Structures of mVDAC1 and mVDAC1-Cys were prepared from the 3EMN crystal structure by
596 aligning the protein to its corresponding *Orientation of Protein in Membranes* (OPM) structure
597 (50). This enabled to translate the system so that its center of mass was positioned at the origin
598 and the pore was oriented along the z axis. In the case of mVDAC1-Cys, the MOE program
599 (46) was used to mutate residues L10 and A170 into cysteines and to create the disulfide bond.
600 The channel was then embedded into a DOPC/DOPE membrane using the CHARMM-GUI
601 membrane builder webserver (51). A rectangular simulation box with TIP3P water was con-
602 sidered. The membrane was built following a 2:1 PC:PE ratio as it was shown to be representa-
603 tive of the lipid composition of the MOM (52). Lipids were positioned in such a way as to
604 roughly cover a 90 x 90 $Å^2$ surface in x and y directions which resulted in 186 lipid molecules.
605 Thickness of water layers on both sides of the membrane was set to 22.5 Å creating around
606 12500 water molecules in the box. Protonation of protein residues was performed with the
607 membrane builder tool. As suggested in Ref. (41), the E73 residue was kept in its unprotonated
608 form although it was initially facing the membrane. A 150 mM-KCl concentration was applied
609 in all our simulations. Finally, equilibration protocol involving minimization, NVT and NPT
610 steps, was similar to the one used for the free peptide except NPT equilibration was run during
611 5ns (mVDAC1) or 10ns (mVDAC1-Cys) using an anisotropic pressure scaling as is required
612 for membrane systems. See "structure preparation (peptide)" for other parameter values.

613 **4.8 Production MD (channel)**

614 All production runs of wild-type mVDAC1 were performed in the NPT ensemble while those
615 related to mVDAC1-Cys were conducted in NVT starting from structures equilibrated in NPT.
616 All our runs were simulated at 150nM KCl concentration. A summary of our exploratory MD
617 and aMD simulations is provided in S2 Table. Transmembrane (TM) potential was modeled
618 by applying an external electric field along the z-axis using Amber's "efz" parameter. Voltages
619 include 0 mV, +40 mV and −40 mV. The reason for running production in NVT was due to
620 the inability of the Amber package to account for virial contribution in NPT upon application
621 of an external field. To investigate the conductance and the stability of mVDAC1-Cys' open
622 state as well as of the 51 subconducting conformers generated from aMD, 200ns-long standard
623 MD trajectories were run at +40mV using each structure as a starting point (one trajectory per
624 conformer). The starting structure in the open state corresponds to our initial structure after 10
625 ns equilibration in NPT (section 4.7). To estimate the electric current, linear regression of the
626 net ion crossing events as a function of time was performed. Since the diffusion coefficient of
627 ions is usually overestimated in MD (29), we first computed the bulk diffusion coefficient of
628 potassium chloride at 10nM as predicted from standard simulation in TIP3P water. A 750ns-
629 long trajectory involving 8 K^+ and 8 Cl^- ions in a box containing around 36700 water molecules
630 resulted in a KCl diffusion coefficient $D_{sim} = 3.273.10^{-5}$cm^2/s ($R^2 = 0.99$) whereas the real
631 diffusion coefficient is known to be $D_{exp} = 1.918.10^{-5}$cm^2/s at the same KCl concentration
632 (53). The D_{exp}/D_{sim} ratio was then used as a multiplicative factor to estimate the current from
633 the slope of the *crossing-events-vs-time* curve.

634 **4.9 GCMC/BD**

635 Poisson-Boltzmann and Poisson-Nernst-Planck (PB/PNP) and GCMC/BD calculations were
636 run using the open-source PB/PNP and GCMC/BD programs available at http://www.charmm-
637 gui.org/?doc=input/gcmcbd. For more details about the PB/PNP and GCMC/BD protocols, see

638 Refs. (27, 54). GCMC/BD simulations were carried out on representative frames of our aMD
639 trajectories of mVDAC1-Cys at 0 mV, +40 mV and −40 mV. RMSD clustering analysis was
640 performed from the full trajectory generated at 0 mV, from 140 ns at +40 mV, i.e., when the
641 N-terminal tail has moved inside the barrel, and from 300 ns at −40 mV. In all cases, 500
642 clusters resulting in 500 frames were generated. Next, the CHARMM-GUI Ion Simulator web-
643 server (55) was used to generate all the input files needed for PB/PNP and GCMC/BD calcula-
644 tions. Each structure was embedded into a 35Å-thick membrane oriented along the z-axis and
645 positioned in the middle of an 85 x 85 x 95 $Å^3$ box. Thickness of buffer regions at the top and
646 bottom of the simulation box were set to 5Å while a fixed concentration of 150-mM KCl was
647 used on both sides of the membrane. PB/PNP was carried out prior to GCMC/BD in order to
648 estimate the protein electrostatic and steric potentials on each point of a rectangular grid with
649 a grid spacing of 0.5Å. These values are used in GCMC/BD simulations. Each GCMC/BD run
650 was performed by conducting one GCMC step every BD step for a total of 5.10^7 BD cycles.
651 Values reported in Fig 5 and S6 Fig were obtained by averaging over 3 independent GCMC/BD
652 replicas. The TM voltage was set to +40 mV for frames extracted from aMD at 0 mV and
653 +40 mV, and to −40 mV for frames extracted from aMD at -40 mV. Conductance was esti-
654 mated by summing up K+ and Cl- currents and dividing by the applied voltage. Anion/cation
655 ratio was computed as the ratio of the Cl- flux to the K+ flux.

656 **Supporting information**

657 **S1 Fig. Convergence of standard MD simulations of the N-terminal peptide.** The figure
658 shows the number of clusters generated as a function of the simulation time in the case of the
659 ff14SB force field (A) and of the ff14IDPSFF force field (B). Clustering analysis was per-
660 formed using a hierarchical agglomerative approach with an RMSD threshold of 3Å.

661 **S2 Fig. PMF profile generated from standard MD simulations of the N-terminal peptide.**
662 PMFs were obtained in the cases of ff14SB (top) and ff14IDPSFF (bottom) and are given as a
663 function of the radius of gyration (R_g) and the RMSD with respect to the N-terminal
664 conformation in the 3EMN crystal structure. Representative structures in main basins and tran-
665 sition regions are also depicted. The top figure was built out of a 1.6 μs-long trajectory while
666 data at the bottom were collected over 2.1 μs.

667 **S3 Fig. PMF profile generated from aMD simulation of the N-terminal peptide with the**
668 **ff14SB force field.** Due the biased nature of the simulation, density values were reweighted
669 from a Maclaurin series up using terms up to rank $k = 10$ (Eq. (5)). As in S2 Fig, the PMF is
670 given as a function of the radius of gyration (R_g) and the RMSD with respect to the N-terminal
671 conformation in the crystal structure of mVDAC1. The dashed dark-blue trajectory represents
672 a 20ns-long aMD trajectory generated by initiating our simulation from a fully unfolded
673 structure (dark blue cross) that clearly shows the convergence to the helix-enriched basin.

674 **S4 Fig. Secondary structure content of wild-type mVDAC1 N-terminus.** Values were ob-
675 tained from 100ns-long MD runs using the ff14SB force field (left) and the ff14IDPSFF force
676 field (right). Note that β-content is not displayed as it is everywhere zero and helical content
677 includes both 3_{10} and regular α-helix content. For both force fields, 3_{10} content is found only
678 in the short helix made of residues TYR7 to ASP9 and regular helix content was only observed
679 in the long helix made of residues LYS12 to THR19.

680 **S5 Fig. Representative conformers of mVDAC1-Cys at 0mV, +40mV and -40 mV.** Con-
681 formers were obtained from agglomerative hierarchical clustering analysis of aMD trajectories
682 using the RMSD of the N-terminus as a metric and a threshold distance of 3.0 Å. Only the 5
683 most populated clusters are shown at each voltage. Bonded L10C and A170C residues are
684 shown in green.

685 **S6 Fig. Conductance and anion/cation ratio of mVDAC1-Cys structures generated from**
686 **aMD at 0mV, +40 mV and -40mV**. All values were obtained from GCMC/BD runs at 150
687 mM KCl concentration performed on 500 representative structures of each aMD trajectory.
688 Time series curves were reconstructed by assigning the same conductance and anion/cation
689 ratio to all the frames of a given cluster. Red stars correspond to all the frames with a conduct-
690 ance less than 0.6 nS or an anion/cation ratio less than 4. Note that the frames extracted from
691 our aMD trajectories at +40mV and -40mV were selected from 140 ns and 300 ns, respectively.

692 **S7 Fig. Subconducting mVDAC1-Cys structures identified from standard MD.** The
693 frames correspond to the rows highlighted in green in S3 Table, namely frames 4, 12, 30, 37
694 and 46. The first cluster (S1 state) is made of frames 30 and 46 while the second cluster is made
695 of frames 4, 12 and 37 (S2 state).

696 **S8 Fig. RMSD in mVDAC1-Cys open state and subconducting S1 state.** The backbone
697 RMSD of the whole channel as well as the RMSD of the T6-G25 segment are shown.

698 **S9 Fig. Application of the s2D method on VDAC N-terminus.** The graph displays random-
699 coil and secondary structure propensity for each residue.

700 **S10 Fig. Hydrogen bonds and hydrophobic contacts in mVDAC1-Cys open state and S1.**
701 Each graph was built out of 25 frames equally spaced in time in each 450ns-long trajectory.
702 Only contacts occurring in 50% of cases or more are depicted. Red squares correspond to hy-
703 drogen bonds while blue squares stand for hydrophobic contacts. Note that contacts are only
704 displayed in the upper left corner of each graph to avoid redundancy. In S1 state, the dashed
705 rectangle includes hydrophobic contacts that stabilize the N-terminus against the barrel wall.
706 Other interactions such as the E84-K115 salt bridge are shown.

707 **S1 Table. RMSE and Pearson correlation coefficient (R) obtained by comparing experi-**
708 **mental and simulated chemical shifts of the N-terminal peptide.** Simulations include MD
709 and aMD ones using either the ff14SB or the ff14IDPSFF force field.

710 **S2 Table. Molecular simulations of mVDAC1 (WT and double Cys mutant) performed**
711 **in the present study.**

712 **S3 Table. Current, conductance and anion/cation ratio of mVDAC1-cys frames selected**
713 **from aMD simulation at +40mV.** The values were predicted by running 200ns-long standard
714 MD for each frame and by recording ion permeation events. The R^2 coefficient obtained from
715 linear regression of the *crossing-events-vs-time* curve is also displayed. The current was com-
716 puted by multiplying the predicted slope of the curve by a scaling factor (section 4.8). Rows
717 highlighted in green correspond to frames displaying both reduced conductance (around 0.6 nS
718 or less) and a low anion/cation ratio (around 4 or less). Frames 30 and 46 correspond to the
719 same structural S1 state while frames 4, 12 and 37 belong to S2 state (S7 Fig). Rows highlighted
720 in orange stand for frames showing only low anion/cation ratio while rows in grey-blue are
721 related to subconducting states with high anion/cation ratio (greater than 4.5).

722 **S1 Video. Clip of the MD trajectory of wild-type mVDAC1 (650 ns) using ff14IDPSFF in**
723 **the absence of applied voltage.** No conformational transition or change in secondary structure
724 content was observed.

725 **S2 Video. aMD trajectory of mVDAC1-Cys (420 ns) at +40mV using ff14SB.** Bonded L10C
726 and A170C residues are shown in green. No conformational transition or change in secondary
727 structure content was observed.

728 **S3 Video. aMD trajectory of mVDAC1-Cys (540 ns) at 0mV using ff14IDPSFF.** Bonded
729 L10C and A170C residues are shown in green. The 3_{10}-helix made of residues Y7, A8 and D9

was found to unfold at 160 ns. However, the position of the N-terminal tail (M1-P5) and of the long helix (K12 to T19) remained unchanged.

S4 Video. aMD trajectory of mVDAC1-Cys (320 ns) at +40mV using ff14IDPSFF. Bonded L10C and A170C residues are shown in green. The 3_{10}-helix made of residues Y7, A8 and D9 was found to unfold at 20 ns. Subsequently, the N-terminal tail (M1-P5) moves further inside the barrel (at 140 ns) leading to steric hindrance of the pore.

S5 Video. aMD trajectory of mVDAC1-Cys (595 ns) at -40mV using ff14IDPSFF. Bonded L10C and A170C residues are shown in green. The 3_{10}-helix made of residues Y7, A8 and D9 was found to unfold at 2 ns.

S6 Video. MD trajectory of mVDAC1-Cys in the open state (450 ns) at +40mV using the ff14IDPSFF force field. Bonded L10C and A170C residues are shown in green.

S7 Video. MD trajectory of mVDAC1-Cys in the S1 state (450 ns) at +40mV using the ff14IDPSFF force field. Bonded L10C and A170C residues are shown in green.

Author Contributions

Conceptualization: Jordane Preto, Isabelle Krimm

Formal analysis: Jordane Preto

Investigation: Jordane Preto

Methodology: Jordane Preto

Resources: Isabelle Krimm

Software: Jordane Preto

Supervision: Isabelle Krimm

Visualization: Jordane Preto

Writing – original draft: Jordane Preto, Isabelle Krimm

754 Writing – review & editing: Jordane Preto, Isabelle Krimm

755

756 **Acknowledgments**. We gratefully acknowledge support from the PSMN (Pôle Scientifique de

757 Modélisation Numérique) of the ENS de Lyon for the computing resources.

758

759 **Competing interests.** The authors have declared that no competing interests exist.

760

761 **References**

762 (1) Shoshan-Barmatz V, De Pinto V, Zweckstetter M, Raviv Z, Keinan N, Arbel N. VDAC, a
763 multi-functional mitochondrial protein regulating cell life and death. Mol Aspects Med 2010
764 June 01;31(3):227-285.

765 (2) Shoshan-Barmatz V, Maldonado EN, Krelin Y. VDAC1 at the crossroads of cell
766 metabolism, apoptosis and cell stress. Cell Stress 2017 October 01;1(1):11-36.

767 (3) Magri A, Reina S, De Pinto V. VDAC1 as Pharmacological Target in Cancer and
768 Neurodegeneration: Focus on Its Role in Apoptosis. Front Chem 2018 April 06;6:108.

769 (4) Bergdoll L, Grabe M, Abramson J. An Assessment of How VDAC Structures Have
770 Impacted Our Understanding of Their Function. Molecular Basis for Mitochondrial Signaling:
771 Springer; 2017. p. 141-160.

772 (5) Colombini M. VDAC structure, selectivity, and dynamics. Biochim Biophys Acta 2012
773 June 01;1818(6):1457-1465.

774 (6) Hodge T, Colombini M. Regulation of metabolite flux through voltage-gating of VDAC
775 channels. J Membr Biol 1997 June 01;157(3):271-279.

776 (7) Bayrhuber M, Meins T, Habeck M, Becker S, Giller K, Villinger S, et al. Structure of the
777 human voltage-dependent anion channel. Proc Natl Acad Sci U S A 2008 October
778 07;105(40):15370-15375.

779 (8) Hiller S, Garces RG, Malia TJ, Orekhov VY, Colombini M, Wagner G. Solution structure
780 of the integral human membrane protein VDAC-1 in detergent micelles. Science 2008 August
781 29;321(5893):1206-1210.

782 (9) Ujwal R, Cascio D, Colletier JP, Faham S, Zhang J, Toro L, et al. The crystal structure of
783 mouse VDAC1 at 2.3 A resolution reveals mechanistic insights into metabolite gating. Proc
784 Natl Acad Sci U S A 2008 November 18;105(46):17742-17747.

785 (10) Schneider R, Etzkorn M, Giller K, Daebel V, Eisfeld J, Zweckstetter M, et al. The native
786 conformation of the human VDAC1 N terminus. Angew Chem Int Ed Engl 2010 March
787 01;49(10):1882-1885.

788 (11) Zachariae U, Schneider R, Briones R, Gattin Z, Demers JP, Giller K, et al. beta-Barrel
789 mobility underlies closure of the voltage-dependent anion channel. Structure 2012 September
790 05;20(9):1540-1549.

791 (12) Geula S, Naveed H, Liang J, Shoshan-Barmatz V. Structure-based analysis of VDAC1
792 protein: defining oligomer contact sites. J Biol Chem 2012 January 13;287(3):2179-2190.

793 (13) Mertins B, Psakis G, Grosse W, Back KC, Salisowski A, Reiss P, et al. Flexibility of the
794 N-terminal mVDAC1 segment controls the channel's gating behavior. PLoS One
795 2012;7(10):e47938.

796 (14) Teijido O, Ujwal R, Hillerdal CO, Kullman L, Rostovtseva TK, Abramson J. Affixing N-
797 terminal alpha-helix to the wall of the voltage-dependent anion channel does not prevent its
798 voltage gating. J Biol Chem 2012 March 30;287(14):11437-11445.

799 (15) De Pinto V, Tomasello F, Messina A, Guarino F, Benz R, La Mendola D, et al.
800 Determination of the conformation of the human VDAC1 N-terminal peptide, a protein moiety
801 essential for the functional properties of the pore. Chembiochem 2007 May 07;8(7):744-756.

802 (16) Guardiani C, Scorciapino MA, Amodeo GF, Grdadolnik J, Pappalardo G, De Pinto V, et
803 al. The N-Terminal Peptides of the Three Human Isoforms of the Mitochondrial Voltage-
804 Dependent Anion Channel Have Different Helical Propensities. Biochemistry 2015 September
805 15;54(36):5646-5656.

806 (17) Maier JA, Martinez C, Kasavajhala K, Wickstrom L, Hauser KE, Simmerling C. ff14SB:
807 Improving the Accuracy of Protein Side Chain and Backbone Parameters from ff99SB. J Chem
808 Theory Comput 2015 August 11;11(8):3696-3713.

809 (18) Song D, Luo R, Chen H. The IDP-Specific Force Field ff14IDPSFF Improves the
810 Conformer Sampling of Intrinsically Disordered Proteins. Journal of Chemical Information and
811 Modeling 2017.

812 (19) Preto J, Clementi C. Fast recovery of free energy landscapes via diffusion-map-directed
813 molecular dynamics. Phys Chem Chem Phys 2014 Sep 28;16(36):19181-19191.

814 (20) Shen Y, Bax A. SPARTA+: a modest improvement in empirical NMR chemical shift
815 prediction by means of an artificial neural network. J Biomol NMR 2010 September
816 01;48(1):13-22.

817 (21) Hamelberg D, Mongan J, McCammon JA. Accelerated molecular dynamics: a promising
818 and efficient simulation method for biomolecules. J Chem Phys 2004 June 22;120(24):11919-
819 11929.

820 (22) Pierce LC, Salomon-Ferrer R, Augusto F. de Oliveira, Cesar, McCammon JA, Walker
821 RC. Routine access to millisecond time scale events with accelerated molecular dynamics.
822 Journal of chemical theory and computation 2012;8(9):2997-3002.

823 (23) Tian C, Kasavajhala K, Belfon KAA, Raguette L, Huang H, Migues AN, et al. ff19SB:
824 Amino-Acid-Specific Protein Backbone Parameters Trained against Quantum Mechanics
825 Energy Surfaces in Solution. J Chem Theory Comput 2020 January 14;16(1):528-552.

826 (24) Villinger S, Briones R, Giller K, Zachariae U, Lange A, de Groot BL, et al. Functional
827 dynamics in the voltage-dependent anion channel. Proc Natl Acad Sci U S A 2010 December
828 28;107(52):22546-22551.

829 (25) Rostovtseva TK, Bezrukov SM. VDAC inhibition by tubulin and its physiological
830 implications. Biochim Biophys Acta 2012 June 01;1818(6):1526-1535.

831 (26) Noskov SY, Rostovtseva TK, Chamberlin AC, Teijido O, Jiang W, Bezrukov SM. Current
832 state of theoretical and experimental studies of the voltage-dependent anion channel (VDAC).
833 Biochim Biophys Acta 2016 July 01;1858(7 Pt B):1778-1790.

834 (27) Im W, Seefeld S, Roux B. A Grand Canonical Monte Carlo-Brownian dynamics algorithm
835 for simulating ion channels. Biophys J 2000 August 01;79(2):788-801.

836 (28) Im W, Roux B. Ion permeation and selectivity of OmpF porin: a theoretical study based
837 on molecular dynamics, Brownian dynamics, and continuum electrodiffusion theory. J Mol
838 Biol 2002 September 27;322(4):851-869.

839 (29) Rui H, Lee KI, Pastor RW, Im W. Molecular dynamics studies of ion permeation in
840 VDAC. Biophys J 2011 February 02;100(3):602-610.

841 (30) Amodeo GF, Scorciapino MA, Messina A, De Pinto V, Ceccarelli M. Charged residues
842 distribution modulates selectivity of the open state of human isoforms of the voltage dependent
843 anion-selective channel. PLoS One 2014 August 01;9(8):e103879.

844 (31) Romero P, Obradovic Z, Li X, Garner EC, Brown CJ, Dunker AK. Sequence complexity
845 of disordered protein. Proteins 2001 January 01;42(1):38-48.

846 (32) Sormanni P, Camilloni C, Fariselli P, Vendruscolo M. The s2D method: simultaneous
847 sequence-based prediction of the statistical populations of ordered and disordered regions in
848 proteins. J Mol Biol 2015 February 27;427(4):982-996.

849 (33) Walsh I, Martin AJ, Di Domenico T, Tosatto SC. ESpritz: accurate and fast prediction of
850 protein disorder. Bioinformatics 2012 February 15;28(4):503-509.

851 (34) Wright PE, Dyson HJ. Linking folding and binding. Curr Opin Struct Biol 2009;19(1):31-
852 38.

853 (35) Meszaros B, Tompa P, Simon I, Dosztanyi Z. Molecular principles of the interactions of
854 disordered proteins. J Mol Biol 2007 September 14;372(2):549-561.

855 (36) Wang W, Ye W, Jiang C, Luo R, Chen H. New Force Field on Modeling Intrinsically
856 Disordered Proteins. Chemical Biology & Drug Design 2014;84(3):253-269.

857 (37) Robustelli P, Piana S, Shaw DE. Developing a molecular dynamics force field for both
858 folded and disordered protein states. Proc Natl Acad Sci U S A 2018 May 22;115(21):E4758-
859 E4766.

860 (38) Best RB, Zheng W, Mittal J. Correction to Balanced Protein–Water Interactions Improve
861 Properties of Disordered Proteins and Non-Specific Protein Association. Journal of Chemical
862 Theory and Computation 2015;11(4):1978.

863 (39) Bohm R, Amodeo GF, Murlidaran S, Chavali S, Wagner G, Winterhalter M, et al. The
864 Structural Basis for Low Conductance in the Membrane Protein VDAC upon beta-NADH
865 Binding and Voltage Gating. Structure 2020 February 04;28(2):206-214.e4.

866 (40) Choudhary OP, Paz A, Adelman JL, Colletier JP, Abramson J, Grabe M. Structure-guided
867 simulations illuminate the mechanism of ATP transport through VDAC1. Nat Struct Mol Biol
868 2014 July 01;21(7):626-632.

869 (41) Briones R, Weichbrodt C, Paltrinieri L, Mey I, Villinger S, Giller K, et al. Voltage
870 Dependence of Conformational Dynamics and Subconducting States of VDAC-1. Biophys J
871 2016 September 20;111(6):1223-1234.

872 (42) Huang J, Rauscher S, Nawrocki G, Ran T, Feig M, de Groot BL, et al. CHARMM36m:
873 an improved force field for folded and intrinsically disordered proteins. Nat Methods 2017
874 January 01;14(1):71-73.

875 (43) Robustelli P, Piana S, Shaw DE. Developing a molecular dynamics force field for both
876 folded and disordered protein states. Proc Natl Acad Sci U S A 2018 May 22;115(21):E4758-
877 E4766.

878 (44) Blachly-Dyson E, Peng S, Colombini M, Forte M. Selectivity changes in site-directed
879 mutants of the VDAC ion channel: structural implications. Science 1990 March
880 09;247(4947):1233-1236.

881 (45) Pearlman DA, Case DA, Caldwell JW, Ross WS, Cheatham TE, DeBolt S, et al. AMBER,
882 a package of computer programs for applying molecular mechanics, normal mode analysis,
883 molecular dynamics and free energy calculations to simulate the structural and energetic
884 properties of molecules. Comput Phys Commun 1995;91(1-3):1-41.

885 (46) *Molecular Operating Environment (MOE)*, 2019.01; Chemical Computing Group ULC,
886 1010 Sherbooke St. West, Suite #910, Montreal, QC, Canada, H3A 2R7, 2020.

887 (47) Karplus M, McCammon JA. Molecular dynamics simulations of biomolecules. Nat Struct
888 Biol 2002 Sep;9(9):646-652.

889 (48) Wang Y, Markwick PR, de Oliveira CA, McCammon JA. Enhanced Lipid Diffusion and
890 Mixing in Accelerated Molecular Dynamics. J Chem Theory Comput 2011 October
891 11;7(10):3199-3207.

892 (49) Miao Y, Sinko W, Pierce L, Bucher D, Walker RC, McCammon JA. Improved
893 Reweighting of Accelerated Molecular Dynamics Simulations for Free Energy Calculation. J
894 Chem Theory Comput 2014 July 08;10(7):2677-2689.

895 (50) Lomize MA, Pogozheva ID, Joo H, Mosberg HI, Lomize AL. OPM database and PPM
896 web server: resources for positioning of proteins in membranes. Nucleic Acids Res 2012
897 January 01;40(Database issue):370.

898 (51) Jo S, Kim T, Im W. Automated builder and database of protein/membrane complexes for
899 molecular dynamics simulations. PLoS One 2007 September 12;2(9):e880.

900 (52) Horvath SE, Daum G. Lipids of mitochondria. Prog Lipid Res 2013 October 01;52(4):590-
901 614.

902 (53) HARNED HS, NUTTALL RL. The diffusion coefficient of potassium chloride in dilute
903 aqueous solution. J Am Chem Soc 1947 April 01;69(4):736-740.

904 (54) Im W, Roux B. Ion permeation and selectivity of OmpF porin: a theoretical study based
905 on molecular dynamics, Brownian dynamics, and continuum electrodiffusion theory. J Mol
906 Biol 2002 September 27;322(4):851-869.

907 (55) Lee KI, Jo S, Rui H, Egwolf B, Roux B, Pastor RW, et al. Web interface for Brownian
908 dynamics simulation of ion transport and its applications to beta-barrel pores. J Comput Chem
909 2012 January 30;33(3):331-339.

910

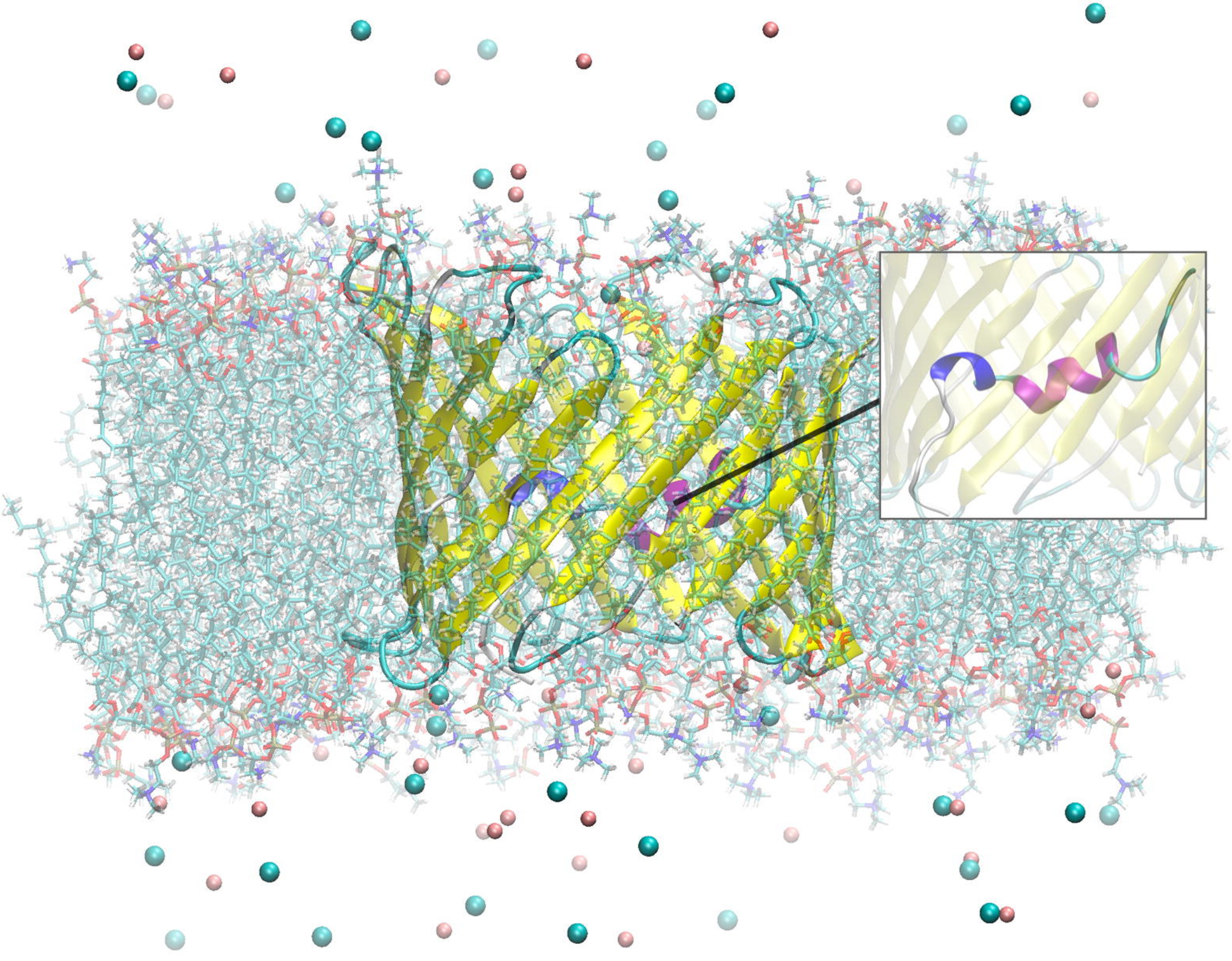

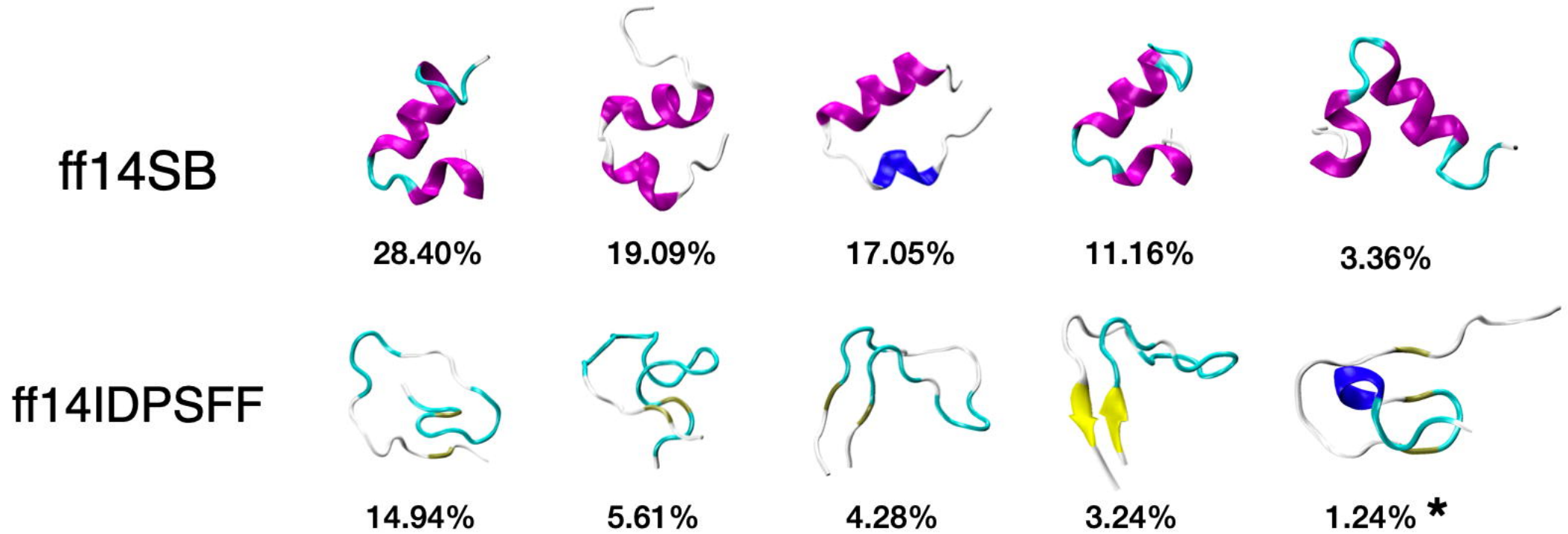
ff14SB
28.40%
19.09%
17.05%
11.16%
3.36%
ff14IDPSFF
14.94%
5.61%
4.28%
3.24%
1.24% *

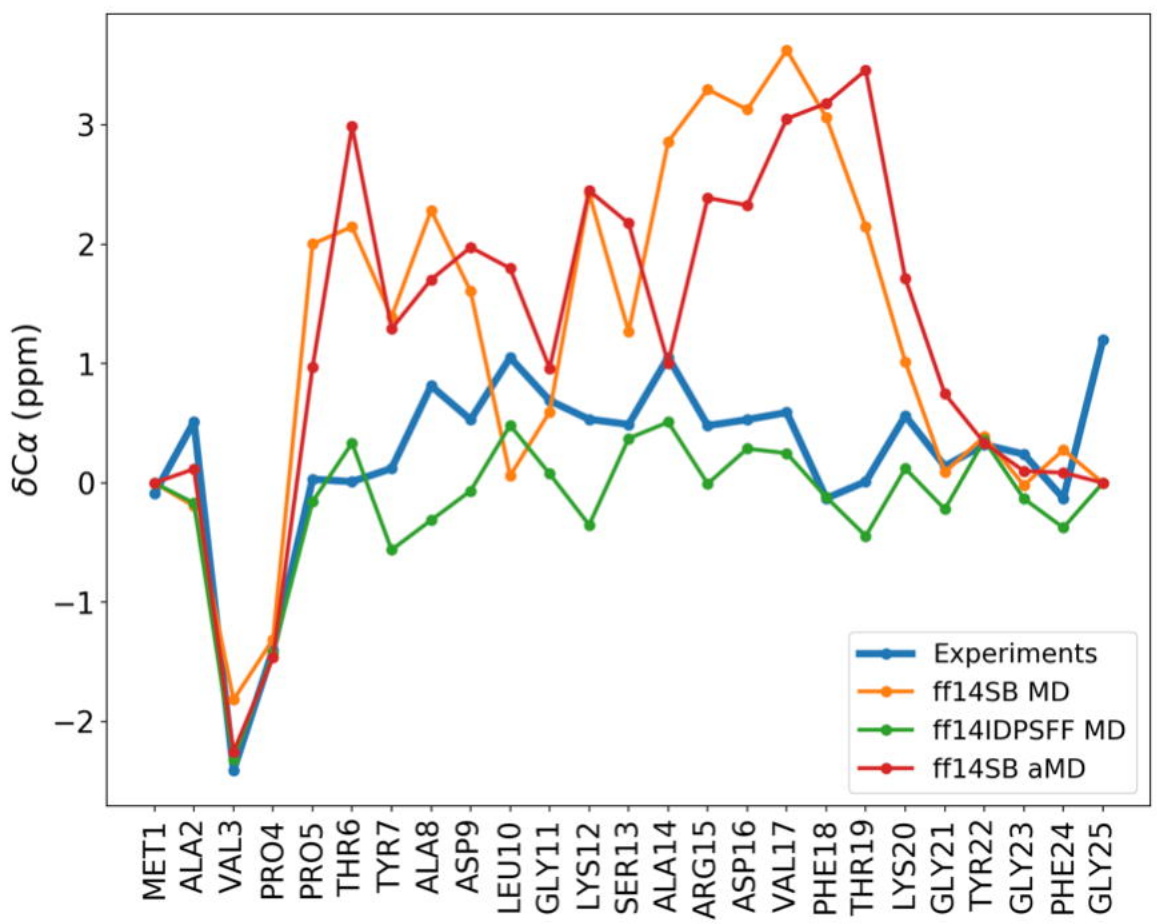
δCα (ppm)
3
2
1
0
−1
−2
Experiments
ff14SB MD
ff14IDPSFF MD
ff14SB aMD
MET1
ALA2
VAL3
PRO4
PRO5
THR6
TYR7
ALA8
ASP9
LEU10
GLY11
LYS12
SER13
ALA14
ARG15
ASP16
VAL17
PHE18
THR19
LYS20
GLY21
TYR22
GLY23
PHE24
GLY25

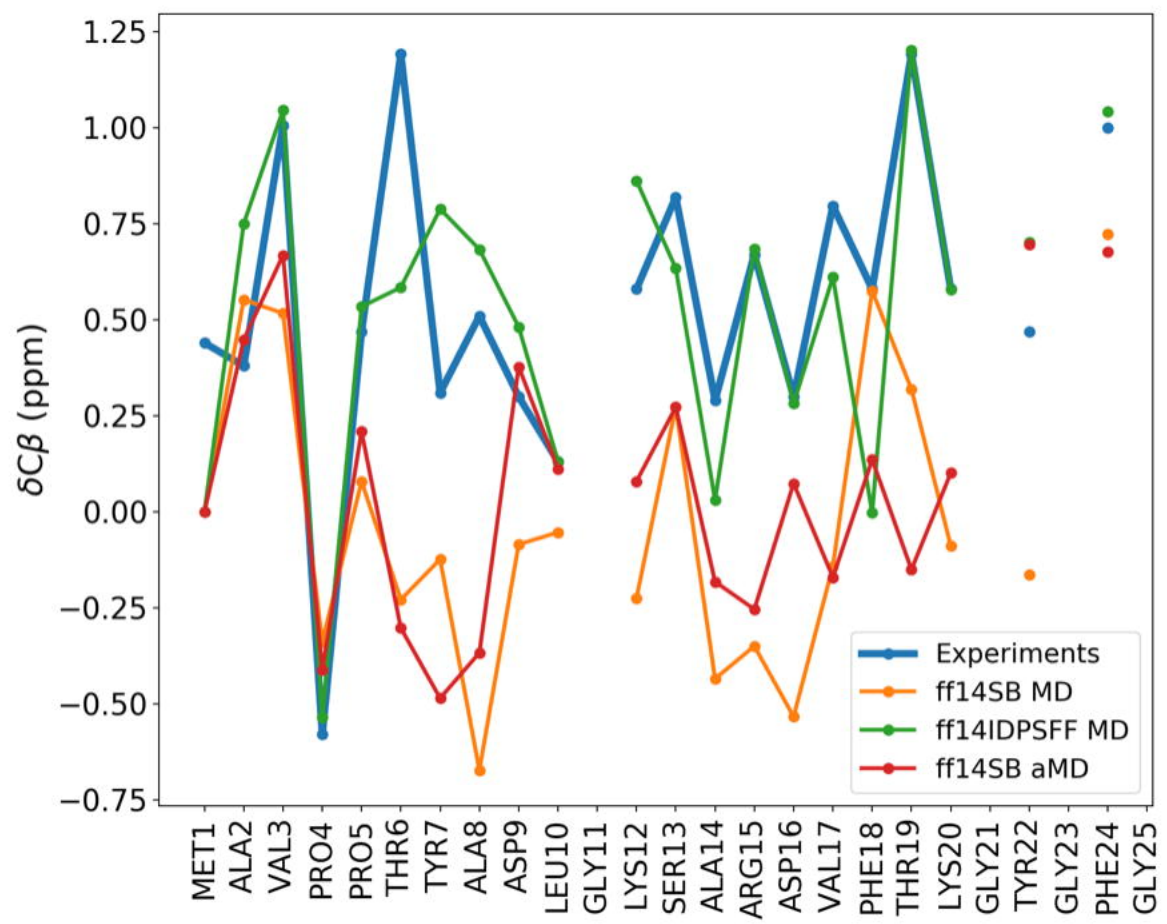
δCβ (ppm)
1.25
1.00
0.75
0.50
0.25
0.00
−0.25
−0.50
−0.75
Experiments
ff14SB MD
ff14IDPSFF MD
ff14SB aMD
MET1
ALA2
VAL3
PRO4
PRO5
THR6
TYR7
ALA8
ASP9
LEU10
GLY11
LYS12
SER13
ALA14
ARG15
ASP16
VAL17
PHE18
THR19
LYS20
GLY21
TYR22
GLY23
PHE24
GLY25

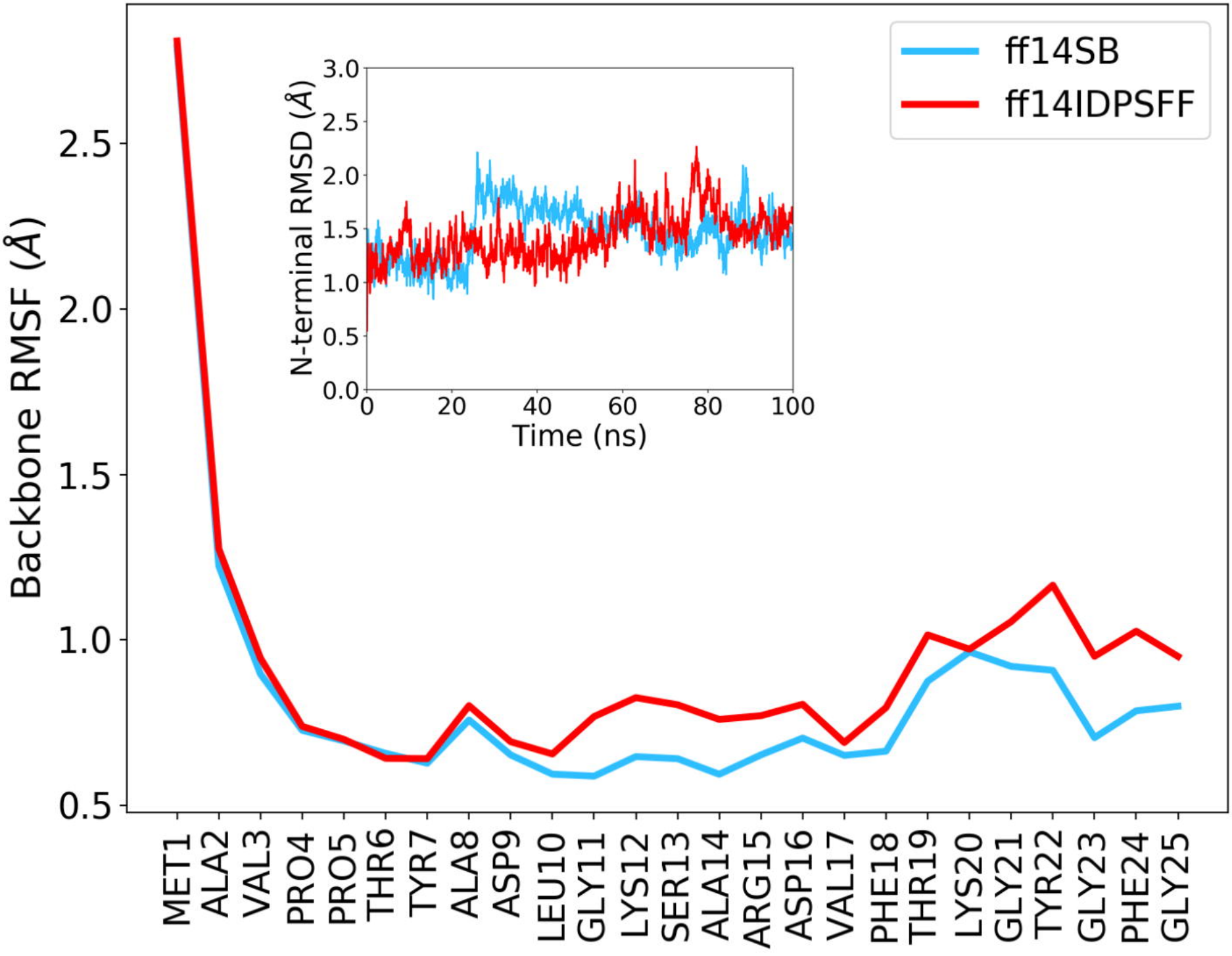
ff14SB
ff14IDPSFF
Backbone RMSF (Å)
2.5
2.0
1.5
1.0
0.5
MET1
ALA2
VAL3
PRO4
PRO5
THR6
TYR7
ALA8
ASP9
LEU10
GLY11
LYS12
SER13
ALA14
ARG15
ASP16
VAL17
PHE18
THR19
LYS20
GLY21
TYR22
GLY23
PHE24
GLY25
N-terminal RMSD (Å)
3.0
2.5
2.0
1.5
1.0
0.5
0.0
0
20
40
60
80
100
Time (ns)

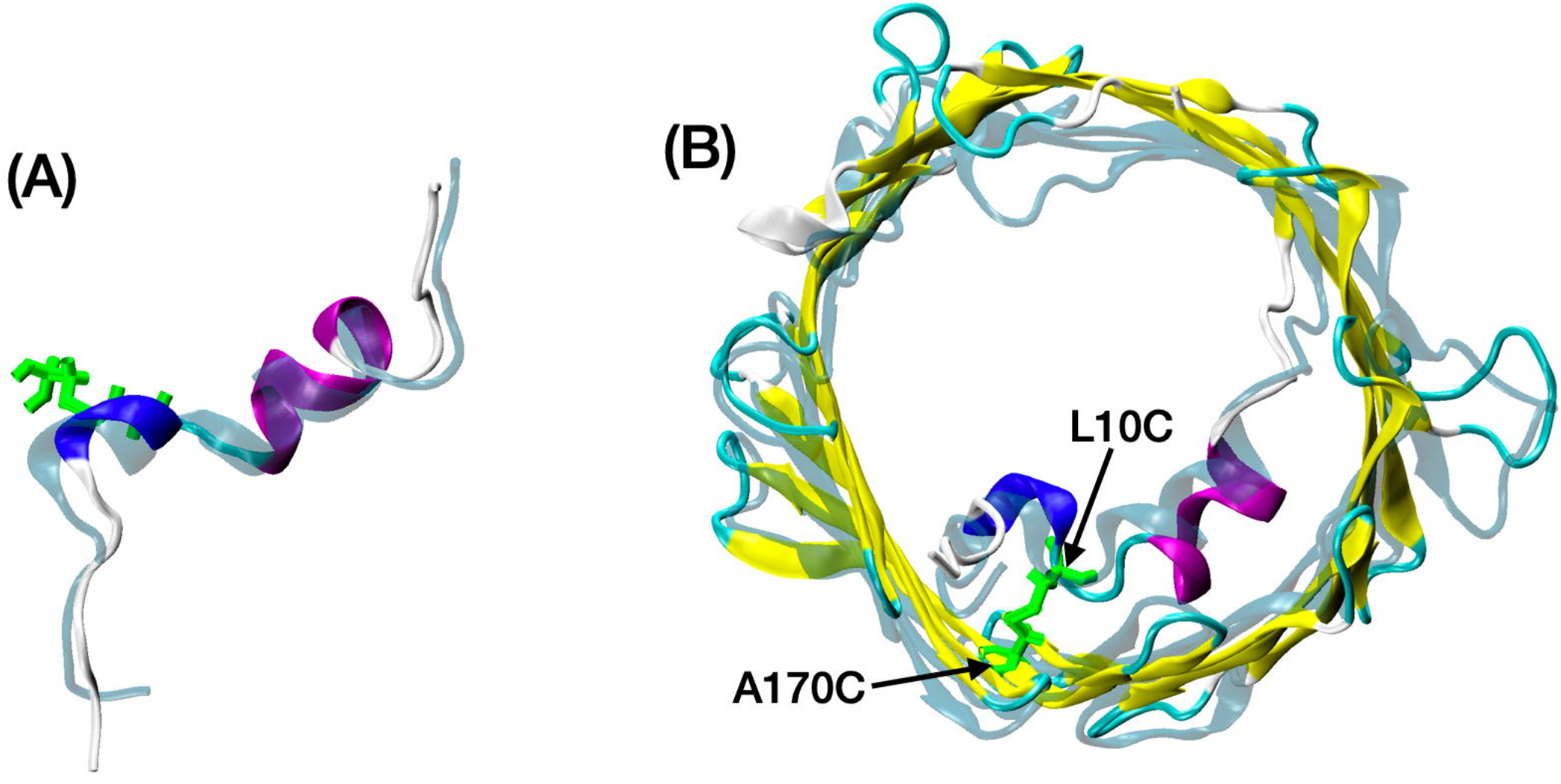
(A)
(B)
L10C
A170C

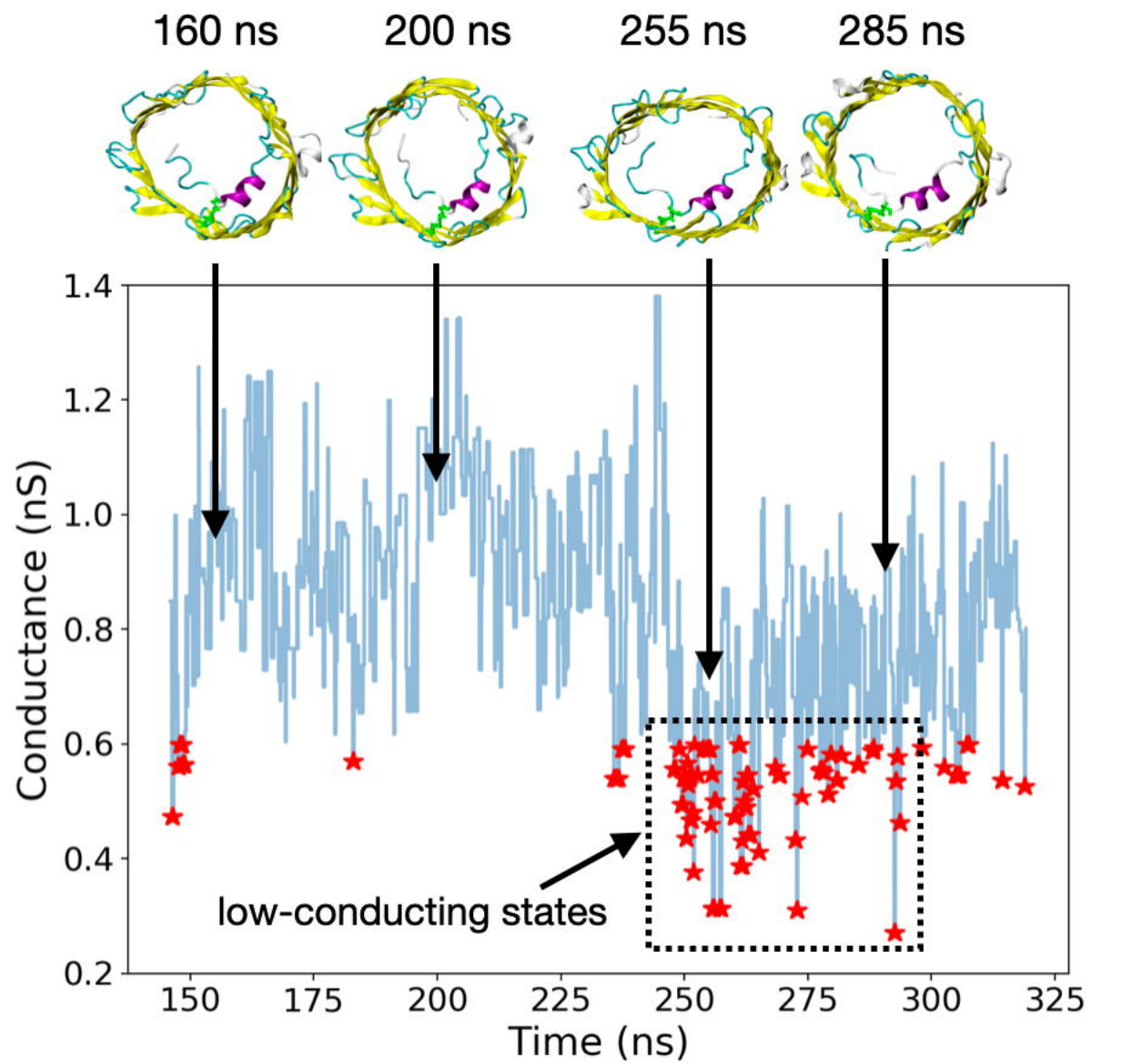
160 ns
200 ns
255 ns
285 ns
Conductance (nS)
1.4
1.2
1.0
0.8
0.6
0.4
0.2
low-conducting states
150
175
200
225
250
275
300
325
Time (ns)

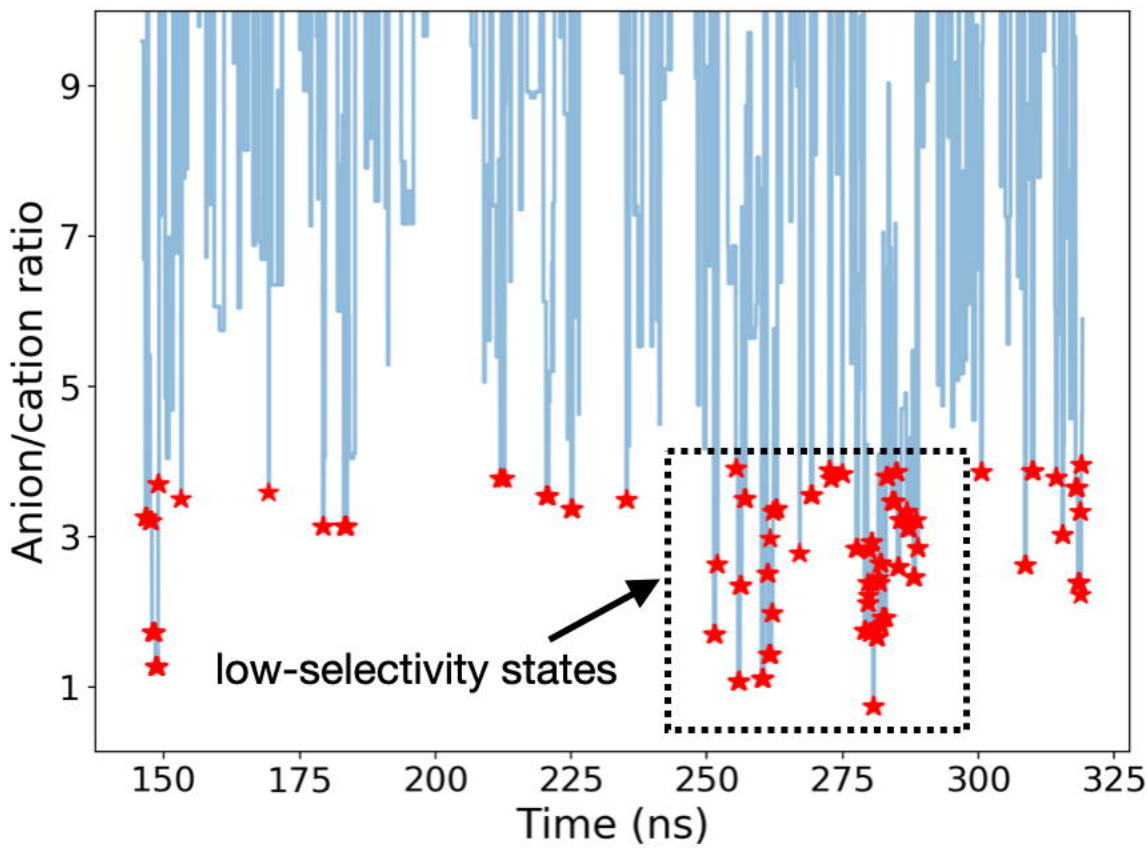
Anion/cation ratio
9
7
5
3
1
low-selectivity states
150
175
200
225
250
275
300
325
Time (ns)

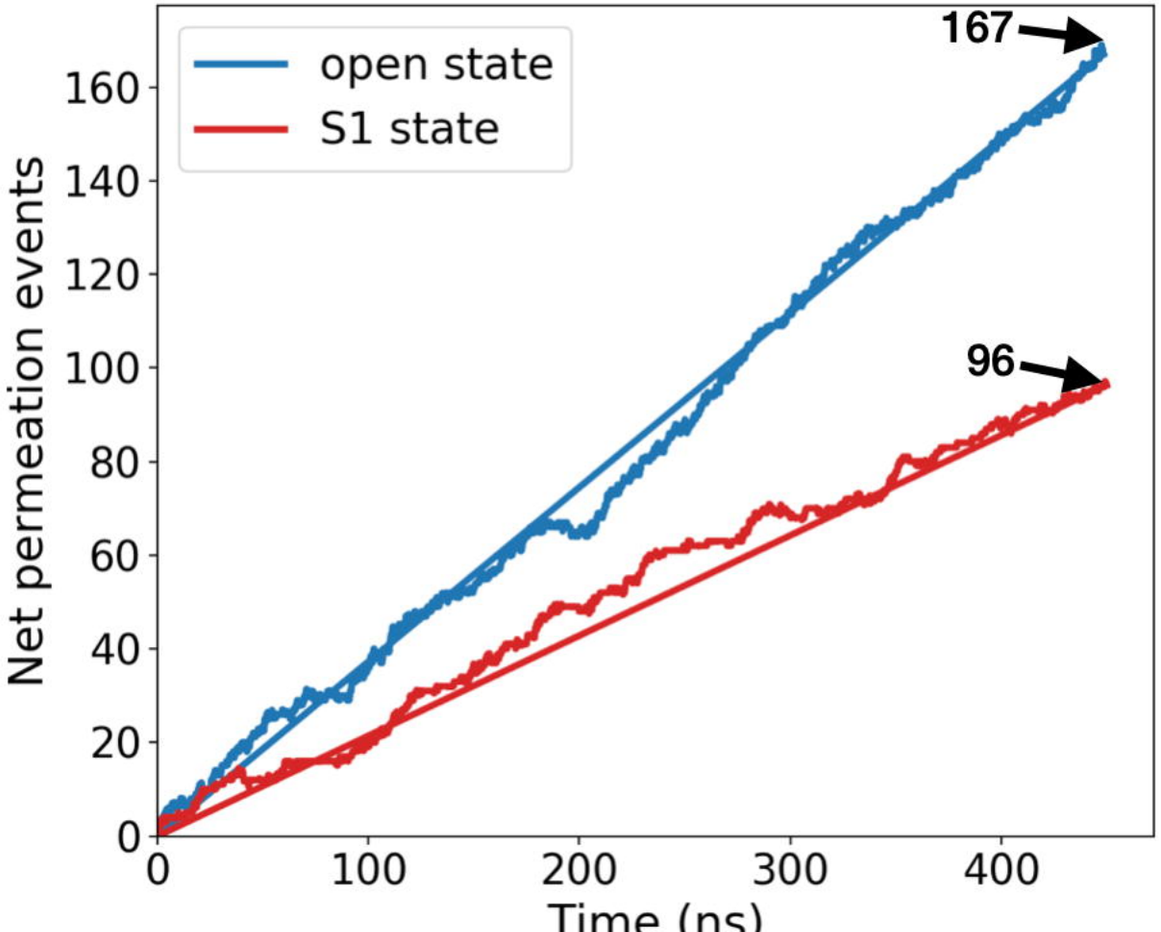
open state
S1 state
167
96
Net permeation events
Time (ns)
0
20
40
60
80
100
120
140
160
0
100
200
300
400

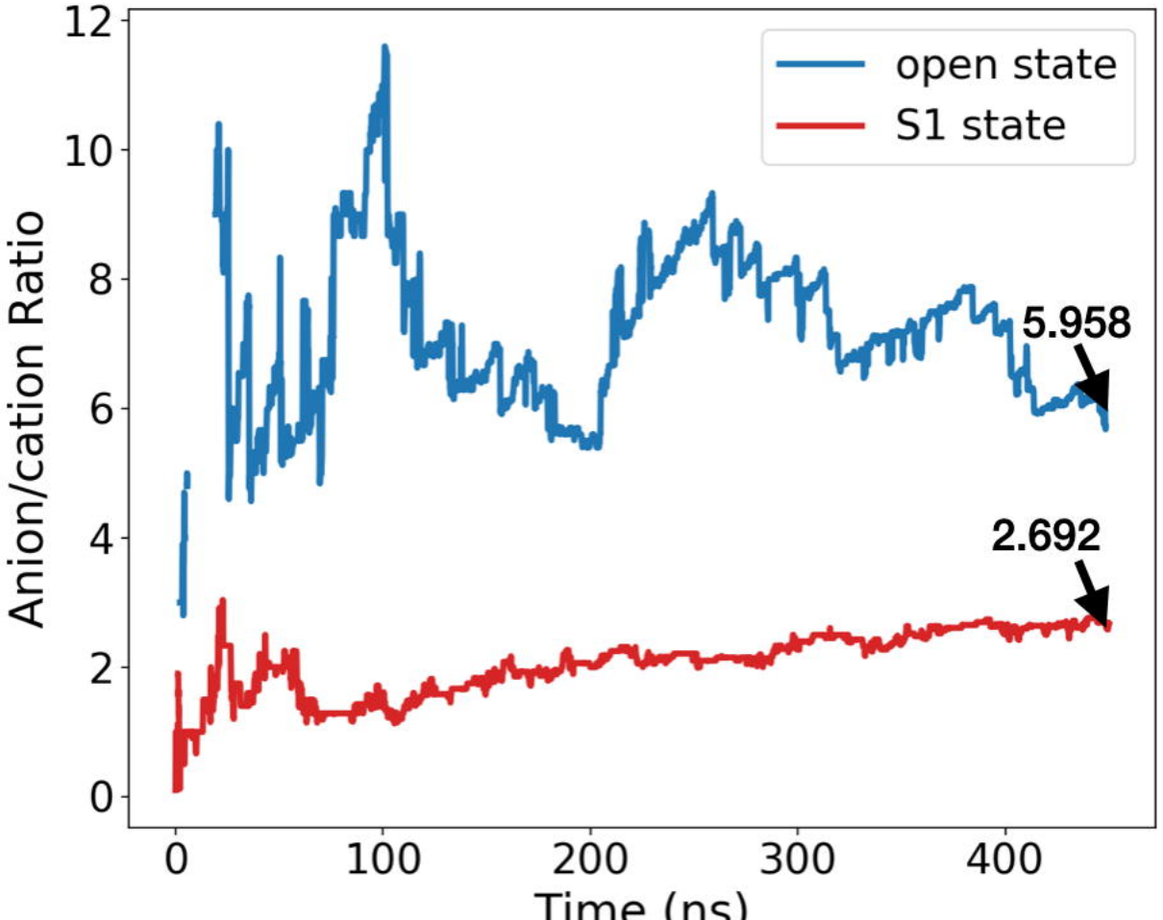
open state
S1 state
5.958
2.692
Anion/cation Ratio
Time (ns)
0
2
4
6
8
10
12
0
100
200
300
400

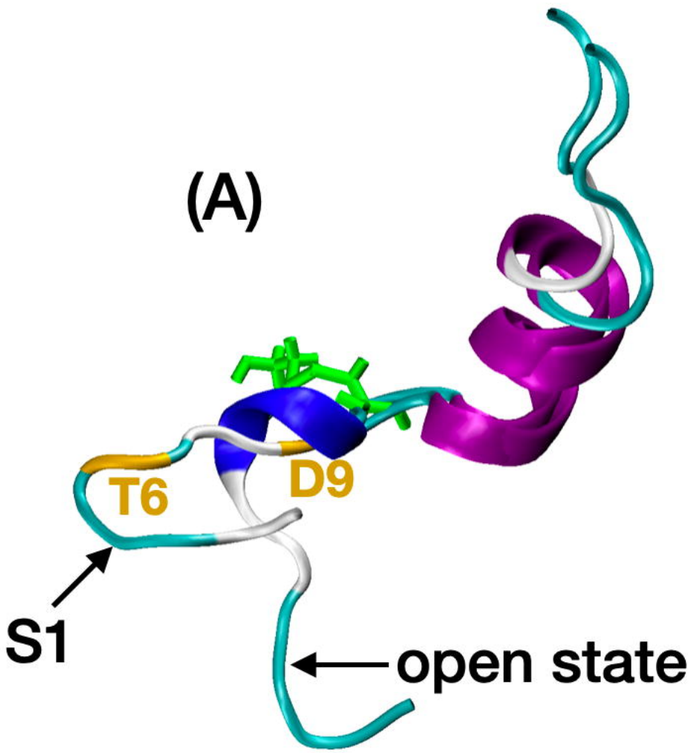
(A)
T6
D9
S1
open state

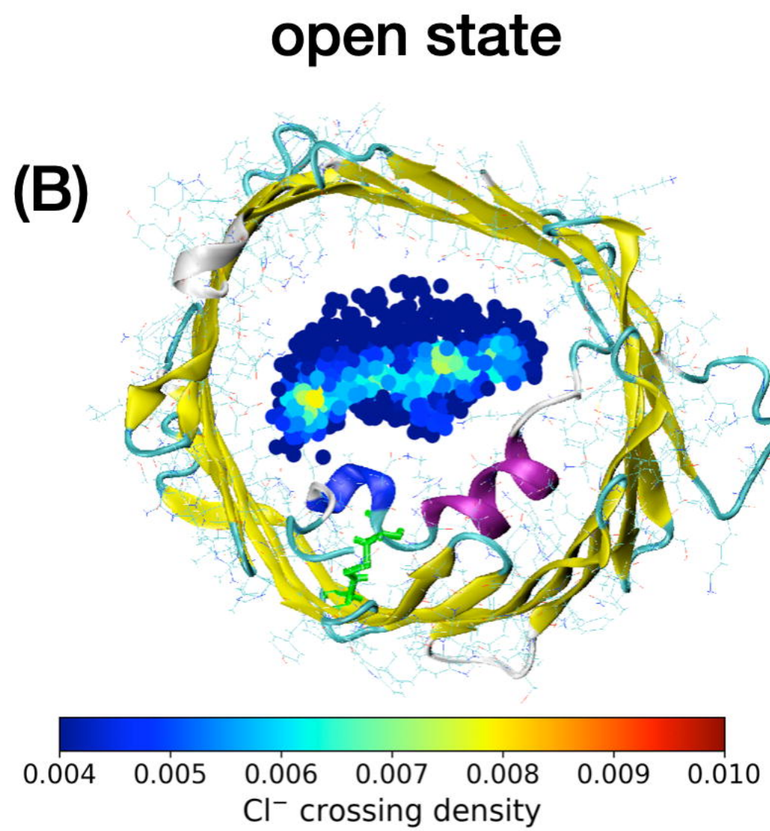
open state
(B)
0.004 0.005 0.006 0.007 0.008 0.009 0.010
Cl⁻ crossing density

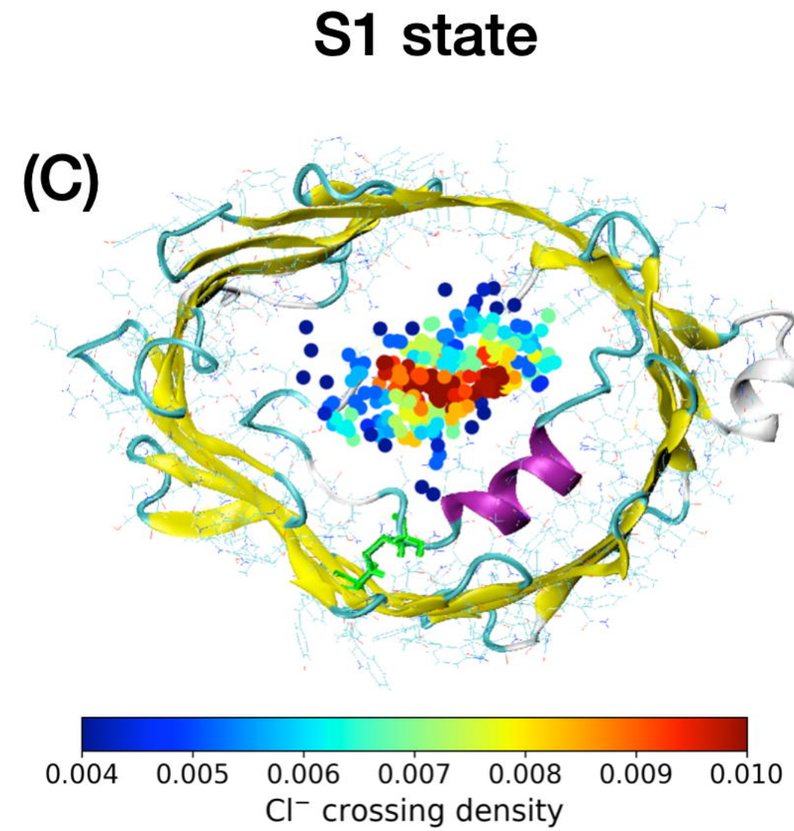
S1 state
(C)
0.004 0.005 0.006 0.007 0.008 0.009 0.010
Cl⁻ crossing density

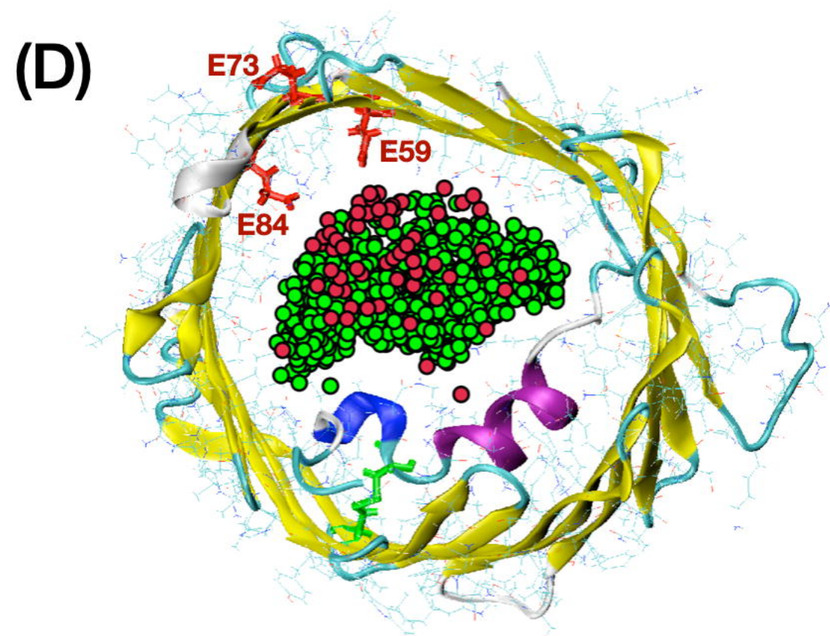
(D)
E73
E59
E84

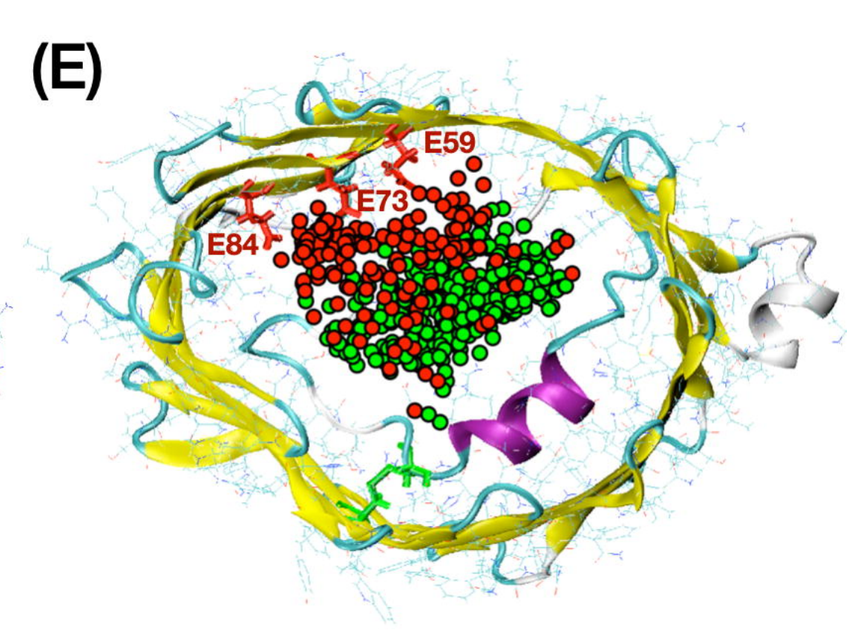
(E)
E59
E73
E84